Spatio-temporally Resolved Magnetic Field Measurements in the ZaP-HD Flow Z-Pinch Device Using Zeeman Splitting

Bennett Diamond

A thesis
submitted in partial fulfillment of the
requirements for the degree of

Master of Science

University of Washington

2022

Reading Committee:
Uri Shumlak, Chair
Justin Little

Program Authorized to Offer Degree:
Aeronautics and Astronautics

University of Washington

Abstract

Spatio-temporally Resolved Magnetic Field Measurements in the ZaP-HD Flow Z-Pinch Device Using Zeeman Splitting

Bennett Diamond

Chair of the Supervisory Committee:
Chair Uri Shumlak
Aeronautics and Astronautics

The ZaP-HD shear-flow-stabilized (SFS) Z-pinch experiment has successfully proven that the instabilities of the simple Z-pinch plasma confinement scheme can be mitigated with sheared flow. Results from ZaP-HD have been used to develop and scale SFS Z-pinches towards high-density and high-temperature fusion conditions. Line radiation spectroscopy has provided insightful, data-rich measurements of a variety of relevant plasma parameters that help generate a greater understanding of the physics of the SFS Z pinch. Although spectroscopy measurements have been taken across the radius of ZaP-HD, these measurements have not been radially deconvolved to give a true picture of the interior of the Z pinch. Ion temperature and magnetic field strength, two critical parameters for better understanding the heating and current flows in ZaP-HD are measured using ion Doppler spectroscopy and Zeeman splitting techniques and are radially deconvolved. Uniform ion temperatures between 10-50 eV and current densities on the order of 50 A/mm^2 are recorded across the radius of the pinch. Spectroscopic measurements of the pinch center and total pinch current are compared to in-situ b-dot probes. Some preliminary time-resolved and deconvolved measurements using a fast-framing ultra high-speed camera are taken and show general agreement with measurements taken by a single-frame ICCD camera.

TABLE OF CONTENTS

Page

LIST OF FIGURES

LIST OF TABLES

ACKNOWLEDGMENTS

I must start by giving a massive thanks to Professor Uri Shumlak for providing excellent advice for this thesis and for also providing excellent professional advice and teaching some fascinating classes on plasma physics. Uri has helped me realize my future goals and has helped me work towards achieving them. I would also like to thank Professor Justin Little for being a member of my committee and also teaching some incredible plasma physics classes.

It would not have been possible to perform any experimentation without the help of the members of the ZaP-HD lab, especially Aqil Khairi, Aria Johansen, Tim Lloyd, and Jared Smythe. My plasma peers must also be acknowledged for their wisdom and support while working on this project. A special thanks must be given to Sari Barczay, Peter Thoreau, Cameron Marsh, and Landon Bevier for being both fun and supportive inside and outside the office.

Finally, I must thank my family and friends for their support and help in making me the person I am today.

Chapter 1

INTRODUCTION

Sustainable energy production is critical to humanity's future as more of the world industrializes, population grows, and climate change becomes an ever worsening reality. One approach currently in development is nuclear fusion, which promises safe, clean, abundant, and politically agreeable energy. Beyond producing energy, fusion also has great promise for enabling crewed deep-space exploration by generating high-energy reactions that close tight mass budgets and reduce long transit windows, limiting harmful radiation exposure [31].

One of the key hurdles for every fusion concept has been confining the energetic ions, electrons, and neutral atoms at high temperatures, high densities, and for long enough periods that enough fusion reactions can occur to offset the large input energies needed to create these conditions. The necessary conditions for fusion reactions, developed by Lawson, are described below for a deuterium-tritium fusion plasma at 20 keV:

$$n\tau = 10^{14}\frac{\mathrm{s}}{\mathrm{cm}^2} \tag{1.1}$$

n is the particle density and τ is the confinement time [22, 33].

Reaching these conditions is not without challenge. Diffusion presents both particle and energy losses while instabilities can rip apart the plasma formation before significant fusion reactions can occur. Significant work has gone into mitigating diffusive losses and instabilities while also increasing plasma parameters to reach the milestone of breakeven [4].

A promising fusion design is the shear-flow-stabilized (SFS) Z pinch. SFS Z pinches increase the stability of the traditional Z pinch while still maintaining the simple, well-understood geometry of the basic Z pinch. This thesis explores the confinement dynamics of the Z pinch through the use of time-resolved and spatially deconvolved spectroscopy to determine magnetic field strength, ion temperature, and plasma current, three parameters critical to the heating, equilibrium, and force balance of the plasma, over the life of the pinch.

1.1 The ZaP-HD Flow Z pinch Experiment

1.1.1 Fundamentals of the Z pinch

Willard Bennett was the first to realize the Z pinch in 1933 [1]. An axial current, by Ampere's Law, generates a magnetic field that radially encompasses and compresses the axial current, "focusing" the plasma into a narrow stream:

$$\nabla \times \boldsymbol{B} = \mu_0(\boldsymbol{J} + \epsilon_0 \frac{\partial \boldsymbol{E}}{\partial t}) \tag{1.2}$$

$\boldsymbol{B}$ is the magnetic field, $\boldsymbol{E}$ is the electric field, μ_0 is the magnetic permeability of free space, ϵ_0 is the permittivity of free space, and J is the current density. The force balance equation best shows how the azimuthal magnetic field provides a confinement force against the outward plasma pressure:

$$\frac{B_\theta}{\mu_0 r}\frac{\partial(rB_\theta)}{\partial r} + \frac{\partial p}{\partial r} = 0 \tag{1.3}$$

p is the plasma pressure and B_θ is the azimuthal magnetic field [30].

Many Z-pinch machines have been developed since the simple geometry and self-induced magnetic field make design and construction affordable. Most designs use two separated electrodes connected to a large capacitor bank with a gas or wire array in between. When the capacitor bank is activated, a large electric field is generated, inducing breakdown and ionization of the wires/gas, generating a current carrying plasma. That current compresses the plasma, generating high plasma temperatures and density [9].

While simple in concept, the Z pinch is susceptible to two forms of instability, the sausage and kink modes, which can destroy confinement before high enough densities and temperatures are reached for large-scale fusion to occur. The sausage ($m = 0$, where m is the mode)

mode develops when one axial region of the pinch is compressed more than surrounding regions. The decreased radius results in a higher current density which in turn creates a large magnetic field that further compresses this necked region. Eventually, the region compresses enough that the plasma is physically cut-off, taking the physical appearance of the sausage links which give the instability its name. The kink ($m = 1$) mode develops from a slight perturbation shifting a section of the pinch off axis. The side of the shifted pinch further from the axis center experiences a reduced magnetic field while the portion closer to the axis experiences an increased magnetic field. This magnetic field gradient further drives the plasma from the axis, eventually kinking the plasma, breaking confinement, and allowing the plasma to dissipate. Figure 1.1 visualizes these two instabilities.

Multiple concepts to mitigate these instabilities, such as the screw pinch and the screw pinch's toroidal nephew the tokamak, have been developed. However, both of these systems rely on advanced and expensive magnets that pose technological and economic difficulties as fusion reactor concepts, and each of these solutions have other caveats that complicate their implementations. The SFS Z pinch, on the other hand, is a simpler concept to build and iterate on.

1.1.2 Z-pinch Stability and Shear-Flow-Stabilization

Plasma instabilities develop when a plasma is not confined in its lowest energy configuration. Any fusion, or high-energy-density plasma, is in an unstable, high energy state since the tightly-confined, hot plasma wants to escape and relax to a lower energy. For Z pinches, the $m = 0$ mode is suppressed when:

$$-\frac{d\ln p}{d\ln r} < \frac{4\gamma}{2+\gamma\beta} \tag{1.4}$$

γ is the ratio of specific heats and β is the ratio of plasma pressure to magnetic pressure [20]. In essence, as long as the pressure does not decrease too rapidly with increasing radius, the pinch will not neck. However, this stability condition places an upper limit on plasma

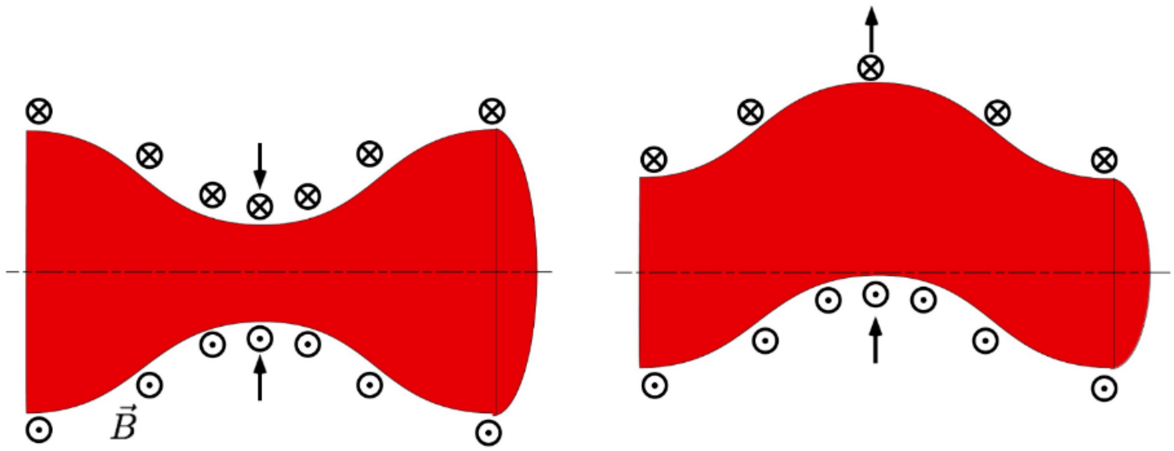

Figure 1.1: $m = 0$ (sausage) and $m = 1$ (kink) mode instabilities, respectively. The red volumes represent the plasma while the density of the circles represent the magnetic field strength [17]. The sausage instability is generated by localized pinching of the plasma. The current density increases in the pinched region resulting in a stronger magnetic field which pinches the region further until the current is cut off and the plasma dissipates. The kink instability is generated from a perturbation that pushes the pinch off axis. The side of the pinch displaced further from the axis has a reduced magnetic field from the convex curvature while the concave curvature of the side that is closer to the axis experiences a larger magnetic field. This magnetic field imbalance drives the pinch from the centerline until the pinch falls apart.

pressure for a certain pinch diameter. As plasma temperatures and number densities reach thermonuclear fusion conditions, the increased plasma pressure violates the stability criteria. A method for mitigating the sausage instability is then needed. The stability criteria for suppressing $m = 1$ modes is also incredibly strict.

$$-\frac{d\ln p}{d\ln r} < \frac{1}{\beta} \tag{1.5}$$

For $\beta > 2\gamma/3$, Eq. 1.5 becomes the limiting stability criteria over Eq. 1.4 and makes reaching stable, long-lived fusion conditions increasingly difficult [20]. Mitigating both the $m = 0$ and $m = 1$ modes is essential.

In 1995, Shumlak and Hartman realized that a sheared-flow, one where the axial velocity of the flow varies with radius, could mitigate the sausage and kink instabilities and allow for continued plasma confinement over many instability growth periods [30]. Any burgeoning instabilities experience destructive interference by the sheared-flow mixing inner and outer layers of the plasma, preventing further instability growth. For shear-flow-stability to take effect, the flow velocity shear must exceed:

$$\frac{dv_z}{dr} \geq 0.1kV_A \tag{1.6}$$

k is the $m = 1$ instability wavenumber and V_A is the Alfvén speed ($V_A = B_\theta/\sqrt{\mu_0\rho}$). This level of shear destroys any growing instabilities, thereby allowing the SFS Z pinch to reach fusion conditions.

Multiple SFS Z-pinch experiments have been built to verify SFS. ZaP was the first of such experimental devices and successfully demonstrated long-lived, stable Z pinches with lifetimes on the order of 40μs, many times the expected instability growth period [29]. Magnetic field probes embedded within the device and a fast-framing camera verified a stable, collimated pinch during the pinch's quiescent period. Axial velocity measurements, performed with ion Doppler spectroscopy, verified a strong, sheared flow that provided the pinch stability. Numerical simulations using the Mach2 resistive MHD code also matched the experimental

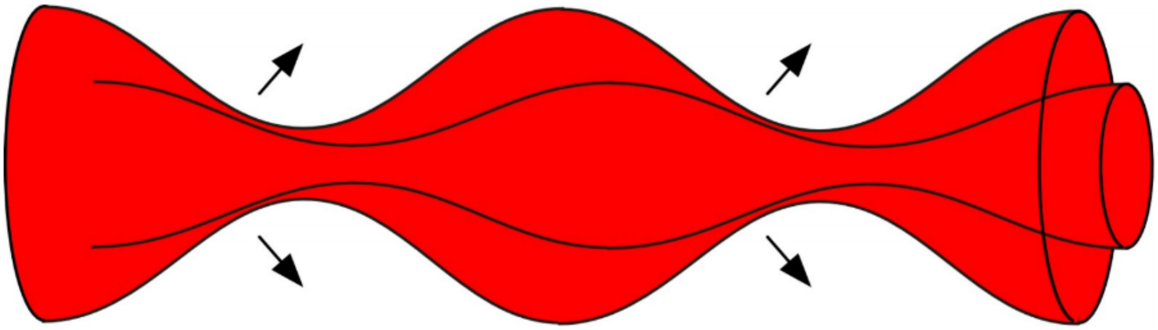

Figure 1.2: Diagram of destructive interference from mixing $m = 0$ instabilities [8].

results. With SFS experimentally proven, ZaP-HD was constructed to demonstrate successful SFS at higher plasma parameters and to increase the machine parameter space by adding a second power supply (discussed in more detail in section 1.1.3). Digital holographic interferometry measurements showed a high-density pinch with a radius of approximately 0.3 centimeters [32]. FuZE was built in the wake of ZaP-HD's success to show that fusion conditions and reactions could be reached by SFS. Neutrons from deuterium-deuterium fusion reactions in the FuZE experiment were recorded by plastic scintillator neutron detectors during peak pinch current, suggesting successful heating and compression of the deuterium plasma to fusion conditions [28]. The results from FuZE demonstrated excellent scaling of plasma parameters, necessary to reach break-even, with increasing pinch. Table 1.1 provides a more complete list of the plasma parameters from the three SFS Z-pinch devices.

1.1.3 The ZaP-HD Shear-Flow-Stabilized Z-pinch Configuration

The experimental machines designed to prove SFS and increase plasma parameters of the SFS Z pinch to fusion conditions consist of two physical sections. The acceleration region is modeled after a Marshall gun [26] and is where the neutral gas is injected, ionized, and fed into the assembly region. In the assembly region, the accelerated plasma is collapsed into

Plasma Parameter	ZaP [29]	ZaP-HD [32]	FuZE [28]
Plasma Current (kA)	100-200	300	300-600
Pinch Current (kA)	50-100	150	150-300
Pinch Radius (cm)	0.5-1	0.3	0.1-0.3
Electron Density (cm^{-3})	10^{16}	2×10^{17}	$> 10^{17}$
Electron Temperature (eV)	80	1000	> 1000

Table 1.1: Comparison of the plasma parameters from three SFS devices. Each of these three devices has successfully demonstrated SFS with ever-increasing plasma parameters. FuZE successfully demonstrated fusion reactions with SFS.

a pinch with the nosecone and end wall serving as the electrodes for the pinch. ZaP, the first SFS Z-pinch machine had two concentric electrodes, aptly named the inner and outer electrodes. The outer electrode encompassed the inner electrode and terminated beyond the end of the inner electrode.

ZaP-HD is the second-generation version of the SFS Z-pinch machine. Unlike its predecessor, ZaP, ZaP-HD is capable of higher densities (hence the HD) and other higher plasma parameters. ZaP-HD's assembly region has two sets of neutral gas injection ports, the inner gas puff port, halfway along the inner electrode, and the outer gas injection ports near the beginning of the acceleration region. ZaP-HD also has 3 electrodes, an inner electrode similar to ZaP, and two outer electrodes, one in the assembly region known as the middle electrode and one in the acceleration region known as the outer electrode. The middle-inner and outer-inner electrode circuits are powered by two separate capacitor banks with separate switches. These two electrodes and power supplies provide more tuneable machine parameters through which to adjust the characteristics of the plasma column.

At the start of the pulse, gas is injected in from both sets of ports. After a small settling time which allows the injected gas to disperse across the annulus of the acceleration

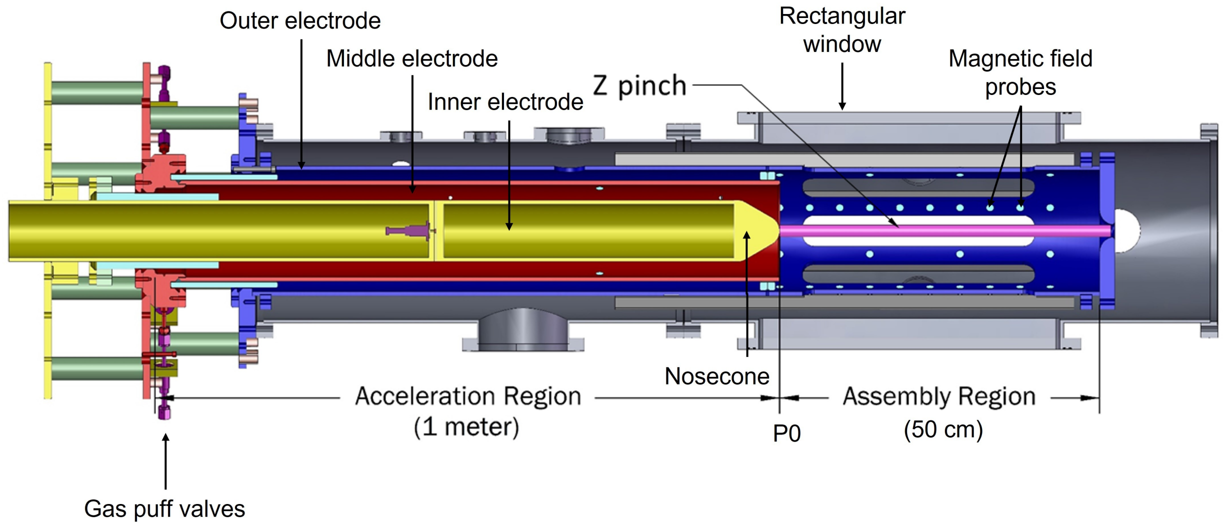

Figure 1.3: CAD drawing of the ZaP-HD SFS Z-pinch machine.

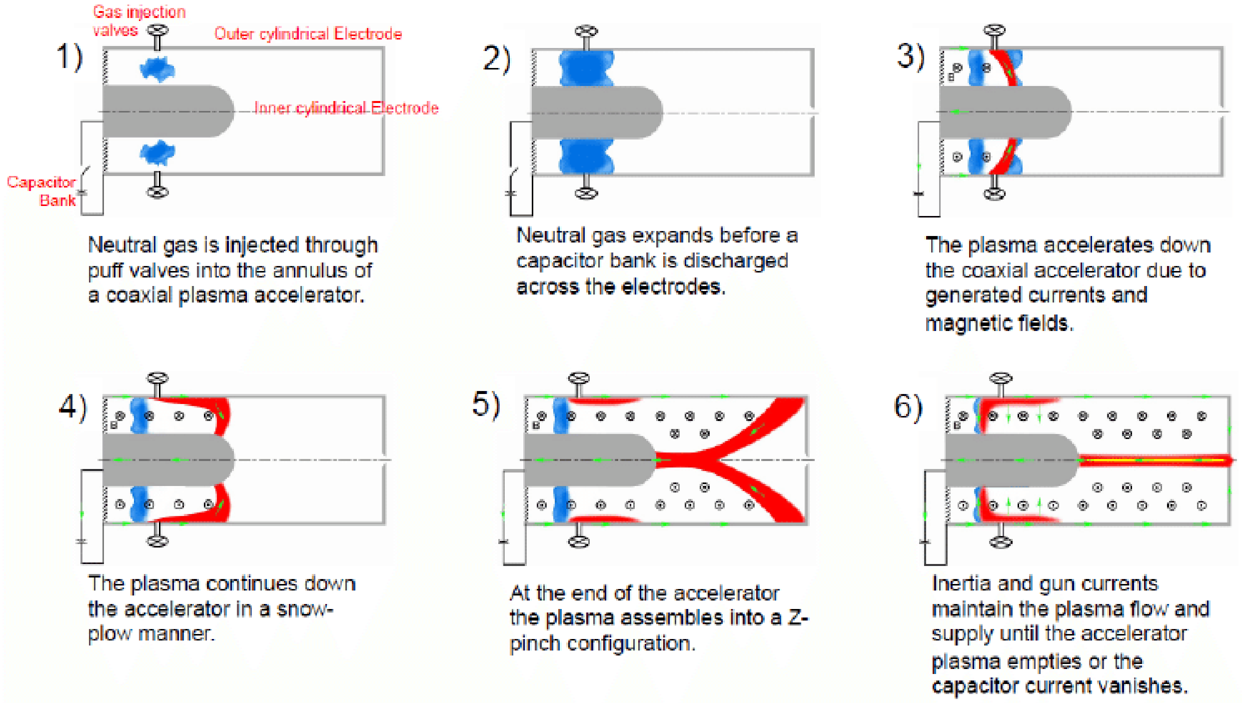

1) Neutral gas is injected through puff valves into the annulus of a coaxial plasma accelerator.

2) Neutral gas expands before a capacitor bank is discharged across the electrodes.

3) The plasma accelerates down the coaxial accelerator due to generated currents and magnetic fields.

4) The plasma continues down the accelerator in a snow-plow manner.

5) At the end of the accelerator the plasma assembles into a Z-pinch configuration.

6) Inertia and gun currents maintain the plasma flow and supply until the accelerator plasma empties or the capacitor current vanishes.

Figure 1.4: The process of SFS Z-pinch formation [35].

region, the acceleration region circuit is closed and the capacitors providing energy to the acceleration region are discharged. The gas in the acceleration region undergoes ionization and begins accelerating by the $\boldsymbol{J} \times \boldsymbol{B}$ force as a snowplow front towards the assembly region. Once the plasma enters the assembly region, the assembly region capacitor bank is activated, energizing the outer electrode. The inner edge of the front remains attached to the nosecone of the inner electrode while the outer edge of the front continues along outer electrode. The azimuthal magnetic field zippers together the stagnating portions of the front to form the pinch. As the rest of the front reaches the end wall, it too stagnates and collapses into the pinch. The moving snowplow front and residual plasma behind the front provide the shear flow needed for sheared-flow stabilization past the stagnated pinch plasma.

1.1.4 Previous Work

Previous Zeeman splitting measurements have been taken on ZaP-HD by McGonigle [24]. However, the focus of his work was more on resolving Stark broadening from Doppler broadening and basic line-integrated Zeeman splitting measurements with some comparison with ZaP-HD's magnetic field probes. This thesis builds off of McGonigle's work by radially deconvolving the Zeeman splitting measurements and comparing the center found through deconvolution with the center found by the magnetic field probes. The radial profile of the magnetic field is also deconvolved. These magnetic field strength measurements are further used to determine the current profile of the pinch. These current measurements are then compared with currents measured by the b-dot probes.

Although temperature measurements are also made in this thesis, Stark broadening is ignored as sensitivity studies conducted after McGonigle's work noted negligible Stark broadening [8]. Therefore, the profile of emitted spectra was assumed to be only Gaussian for this work, removing the need to Fourier transform spectra to better resolve the convolved Stark and Doppler broadening as done by McGonigle and Vogman [34].

McGonigle's measurements were also done with only a single-frame intensified charge-coupled device (ICCD) camera. Measurements for this thesis were made with both a single-frame ICCD camera and a multi-frame ultra-high speed camera which is capable of capturing the temporal evolution of the Z pinch over a single pulse. With a single-frame camera, many pulses would have to be taken to with slightly delayed timings for each frame to capture the evolution of the pinch. Since shot to shot repeatability can be challenging and instabilities are a chaotic process, the single-frame camera cannot effectively capture the temporal evolution of the plasma. Multi-frame cameras, on the other hand, allow for this evolution to be seen in a single pulse.

Chapter 2

ZAP-HD DIAGNOSTICS

2.1 Spectroscopy

Spectroscopy provides significant utility to plasma physicists as plasma emits many forms of radiation with important information about various plasma parameters. Additionally, many spectroscopy detection schemes are non-intrusive, allowing measurement without affecting the plasma itself. For this thesis, line radiation emitted by impurities in the plasma was examined to provide information about magnetic field strength and ion temperature.

Line radiation is emitted by energetic, bound electrons emitting photons as they transition from a higher to lower energy orbital. The wavelength of the radiation emitted by a transition is unique to the ionization state of the ion and the specific orbitals being transited between and is described below:

$$\Delta E = \frac{\hbar}{\lambda} \tag{2.1}$$

ΔE is the energy difference between the two energy states, $\hbar$ is Planck's constant, and λ is the wavelength of the emission. Higher energy transitions will emit at a shorter wavelength and vice versa for lower energy transitions.

For hydrogen plasmas, line radiation spectroscopy becomes quite challenging since ionized hydrogen does not have any bound electrons. A common solution is to introduce impurity atoms, which are not fully ionized and generally exhibit the same bulk motion and are thermalized with the bulk hydrogen plasma. Popular impurities include carbon, nitrogen, and oxygen which can be quite easily introduced either by intentional doping of the input hydrogen gas or as side effects of imperfect vacuums and plasma-material interactions. These elements are abundant, can be readily injected in gaseous form (carbon in the form

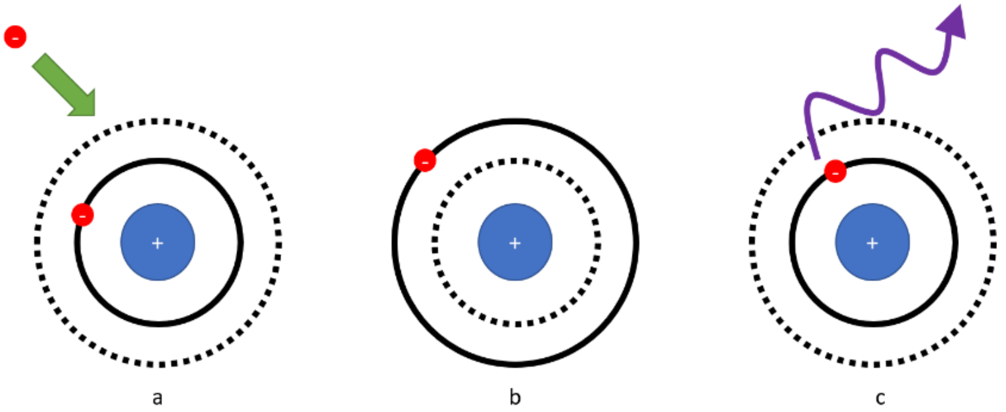

Figure 2.1: A diagram showing the life of an excited electron. a. An excitation event occurs. In this case, a high-energy, free electron interacts with a relaxed, bound electron. b. The bound electron is excited to a higher energy orbital. c. The bound electron relaxes back to its ground state, releasing the excitation energy in the form of a photon [8].

of methane), and have an ideal number of ionization states – enough to not be fully ionized except for the highest temperature plasmas, but not too many as to create a ”forest” of spectra where discerning individual spectra is difficult from many possible transitions. For this thesis, the hydrogen gas normally used for ZaP-HD is doped with significant concentrations of methane to provide bright carbon lines that can be used for analysis. Additional carbon is also introduced to the plasma through plasma sputtering and sublimation of the graphite nosecone [21].

2.1.1 Zeeman Splitting

The influence of a magnetic field on line radiation was first recognized by Zeeman in 1897 [36]. External magnetic fields applied to an atom change the magnetic moment and split the electron orbital energy levels into a series of energy levels above and below the non-magnetized energy level. When bound electrons in a magnetic field transition to a lower energy level,

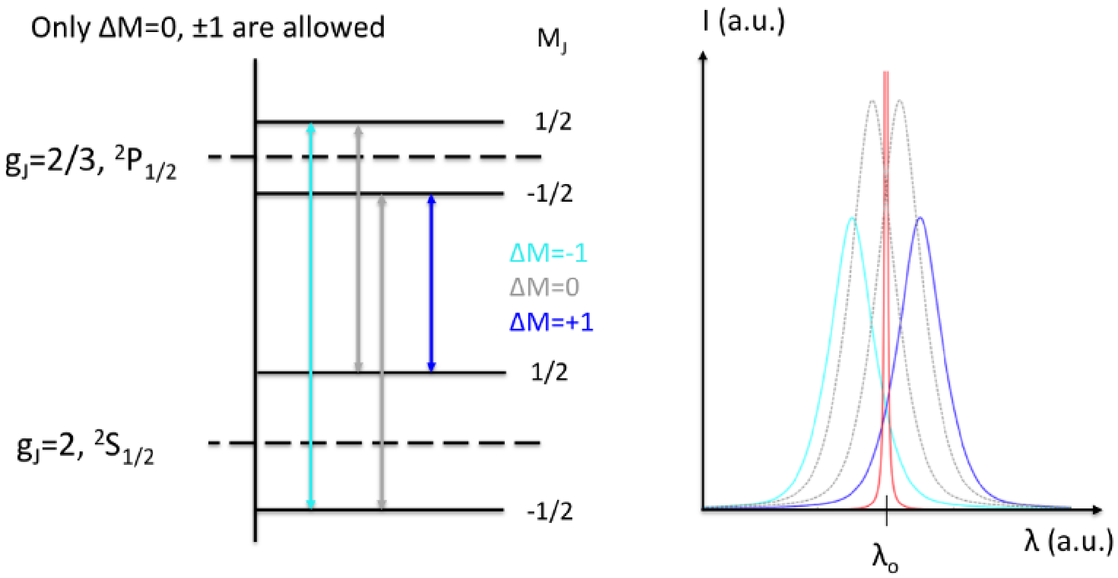

Figure 2.2: Diagrams showing the Zeeman effect for the 581 nm C IV line. The left diagram shows the energy levels of the Zeeman split line. The dotted lines show the demagnetized energy states while the solid lines show the split states. The right diagram shows the Zeeman split in wavelength space. The red distribution is the demagnetized, un-broadened 581 nm line. The blue and turquoise distributions note the $\pm\sigma$ components and the gray distributions note the $\pm\pi$ components [24].

the resulting emission is no longer a single wavelength but a few different wavelengths with wavelengths close to the non-magnetized "center" wavelength, known as π components, and more shifted lines further from the center wavelength known as σ components [16]. Figure 2.2 gives a clear picture of the energy levels and components that make up Zeeman splitting.

For small to medium-strength magnetic fields, the weak-field approximation can be used, and the split in energy states can be described as:

$$\Delta E_B = \mu_B B(g'_J M' - g_J M) \tag{2.2}$$

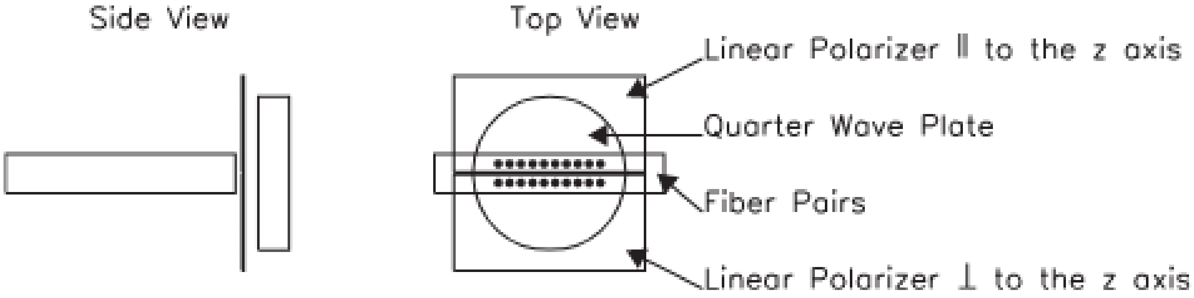

Figure 2.3: Polarizer setup for resolving the σ components of the Zeeman split into two separate fiber bundles for easy analysis [11]. The quarter-wave plate is rotated 45 degrees to the machine axis and linearly polarizes the circularly-polarized σ components. The now linearly-polarized σ components end up rotated 90 degrees from one another. Two linear polarizers rotated orthogonally from one another allow only one of the two σ components to pass into each fiber bundle. The individual σ components are easier to resolve separately than together.

μ_B is the Bohr magnetron, g_J is the Landé g-factor, M is the magnetic moment, and B is the magnetic field strength [27]. ΔE can be found by looking at the wavelength shift of the σ components:

$$\Delta\lambda_B \approx -\frac{\lambda_0^2}{\hbar c}\Delta E_B \tag{2.3}$$

λ_0 is the unshifted wavelength and c is the speed of light [27]. Since the Zeeman split can be quite small, a long-wavelength line is usually analyzed, as maximizing λ_0 will increase the apparent Zeeman split.

The π component can make resolving the shifted σ components quite difficult, especially when the magnetic field is quite weak, as the π component, especially in Stark-broadened plasmas, will hide the σ components. Therefore, suppressing or removing the π component completely can greatly help with analysis [22].

Babcock developed a solution to this problem by only looking at the circularly polarized components from the emission which happen to also be the σ components [19]. A quarter wave plate will circularly polarize linearly polarized light and will linearly polarize circularly polarized light (depending on the phase of the light and orientation of the quarter wave plate). Each σ component is either left hand or right hand circularly polarized, and the polarization of each component after passing through the quarter-wave plate is linearly polarized and orthogonal to one another. The π component, however, becomes circularly polarized when passing through the quarter wave plate. A linear polarizer after the quarter wave plate removes all the now circularly polarized π component. By having two sets of collection optics each with a linear polarizer rotated 90 degrees to the other polarizer, only one of the σ components is seen by each set of optics, deconvolving all the Zeeman components into their individual components for easy analysis [24].

2.1.2 Doppler Shift and Broadening

The Doppler effect, discovered by Doppler in 1842 [5] describes the frequency shift of a wave emitted by a source traveling with some component away from or towards the observer. The Doppler shift is:

$$\Delta v = v - v_0 = \frac{v_0 v}{c} \tag{2.4}$$

v is the particle velocity along the light of sight [16].

When the emitting source moves towards the observer, wavelength decreases as the emitted wave fronts move closer together, and vice-versa for the emitting source moving away from the observer. For optically emitting plasmas, the Doppler shift from their emissions provides insights about plasma temperature and plasma bulk velocity.

A plasma, by the Boltzmann H-Theorem, will settle into a Gaussian/Maxwellian distribution over the thermalization period of the plasma species. The Maxwellian of species s in one dimension takes on the form:

$$f_s(v) = n_s(\frac{m_s}{2\pi k T_s})^{\frac{3}{2}} \exp[-\frac{m_s(v - v_0)^2}{2kT_s}] \tag{2.5}$$

n_s is the number density, m_s is the species' mass, k is Boltzmann's constant, T_s is the temperature, v is the velocity of an individual particle, and v_0 is the bulk (average) velocity of the plasma [13]. Temperature can be found by looking at the full-width at half-maximum (FWHM) of the Maxwellian in wavelength space:

$$\Delta\lambda_{FWHM} = 2\sqrt{2\ln 2\frac{kT_s}{m_s c^2}}\lambda_0 \tag{2.6}$$

$\Delta\lambda_{FWHM}$ is the FWHM of the Maxwellian in wavelength space and λ_0 is the unshifted wavelength [8]. Since Doppler shift is directly related to an emitter's velocity, the Maxwellian distribution of a thermalized plasma in velocity space maps to a Maxwellian distribution in wavelength space when looking at the light emitted from the plasma:

$$f_M(\lambda) = \frac{I}{\sqrt{2\pi}\sigma} \exp[-\frac{(\lambda - \lambda_0 - \boldsymbol{v_0}\lambda_0/c)^2}{2\sigma^2}] \tag{2.7}$$

The bulk velocity as seen in wavelength space is a function of the mean wavelength while the temperature in wavelength space is a function of the FWHM [15]. Notably, neither temperature nor bulk velocity are a function of the same variable. As a result, temperature and bulk velocity can be resolved separately.

2.2 Radial Deconvolution

Spectroscopic optics collect all the light seen along a viewing chord. This makes discerning radially varying plasma parameters difficult as different regions of the plasma with different plasma parameters will be integrated together into the total light seen by the chord. In Z pinches, plasma parameters vary radially from the center of the Z-pinch axis, resulting in concentric "shells" of similar plasma parameters. Looking at the plasma parameters closer to the center of the pinch requires looking "through" the spectra of the outer shells.

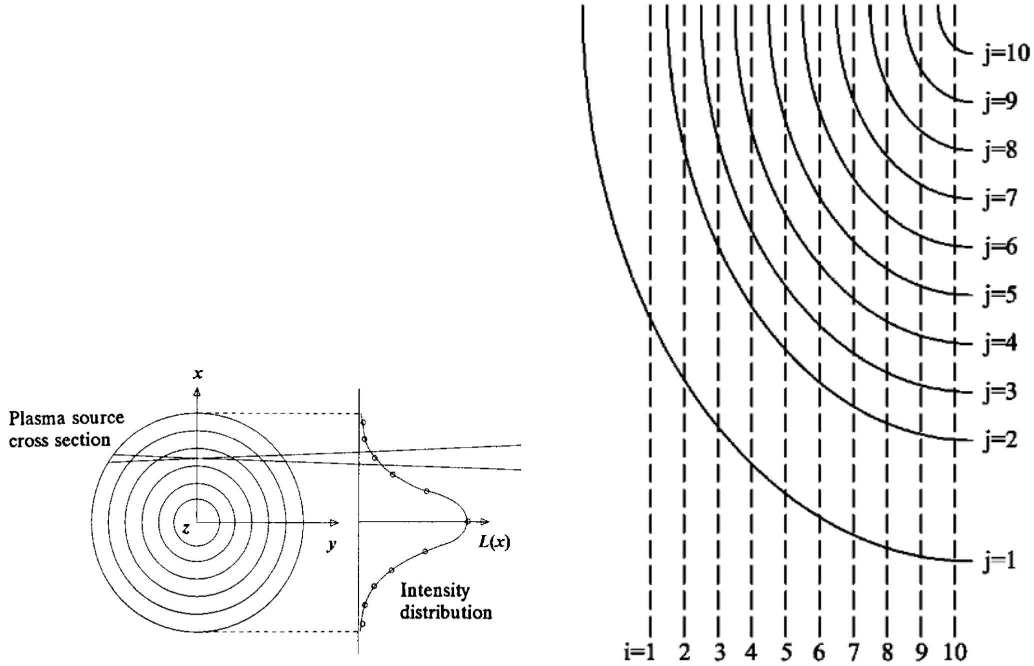

(a) (b)

Figure 2.4: a. A diagram showing the growth in line intensity as more of the plasma is viewed. To determine the intensity of each shell, deconvolution must be used [25]. b. A diagram of concentric shells of plasma (solid lines labeled as j) intersected by viewing chords (dotted lines labeled as i). Note that the viewing chord imaging the center of the plasma also images all the other shells as well. The shells are elliptical as the view is tilted 35 degrees from perpendicular [10].

The process of deconvolution has been used in many plasma experiments to parse out a variety of line-integrated measurements. Generally, an Abel inversion is used: the geometry of the "shells" of the plasma is assumed based on the general geometry and location and angle of the viewing chords relative to the plasma. The center and edges of the plasma are guessed through intensity measurements where the brightest chord defines the center and the zero crossing point of intensity defines the plasma edge. A length matrix defining the length of each viewing chord through each shell of the plasma is then created. The outer chord is fitted to, then a proportion of that fit equal to the percentage of outer shell length in the inner chords is subtracted off, effectively "removing" the outer shell's spectra from the inner shells. The process is repeated with the next outer shell until all shells have had any outer shell influence subtracted off. This scheme is preformed on both sides of the center of the pinch axis and each side's calculations are compared. Since the plasma is assumed to be axisymmetric, any difference in calculated plasma parameters between the two sides means that the center and edges were incorrectly chosen. The center and edges are then adjusted, the length matrix recalculated, and scheme repeated until the calculated parameters from both sides converge [18]. The end result gives the variation of plasma parameters as a function of radius.

When instrument effects such as off-axis wavelength shift and instrument broadening (known collectively as the instrument function) are introduced, an Abel inversion cannot be used as the instrument function must be removed for accurate determination of the plasma parameters. A deconvolution process described by Golingo and Shumlak is instead used [10]. Similarly to an Abel inversion, a length matrix is created for the length of each viewing chord through each shell of the matrix. However, the fit includes instrument broadening and wavelength shift, which are dependent on location on the image sensor:

$$e_{ij}\lambda = \frac{A_j}{\sqrt{2\pi}\sigma_j}\exp[-\frac{(\lambda-\lambda_0-\Delta\lambda_k)^2}{2\sigma_j^2}] + B_j \tag{2.8}$$

λ_0 is the instrument-corrected wavelength, $\Delta\lambda_k$ is the wavelength shift due to Zeeman splitting, and σ_j is the combined instrument temperature and plasma Doppler broadening

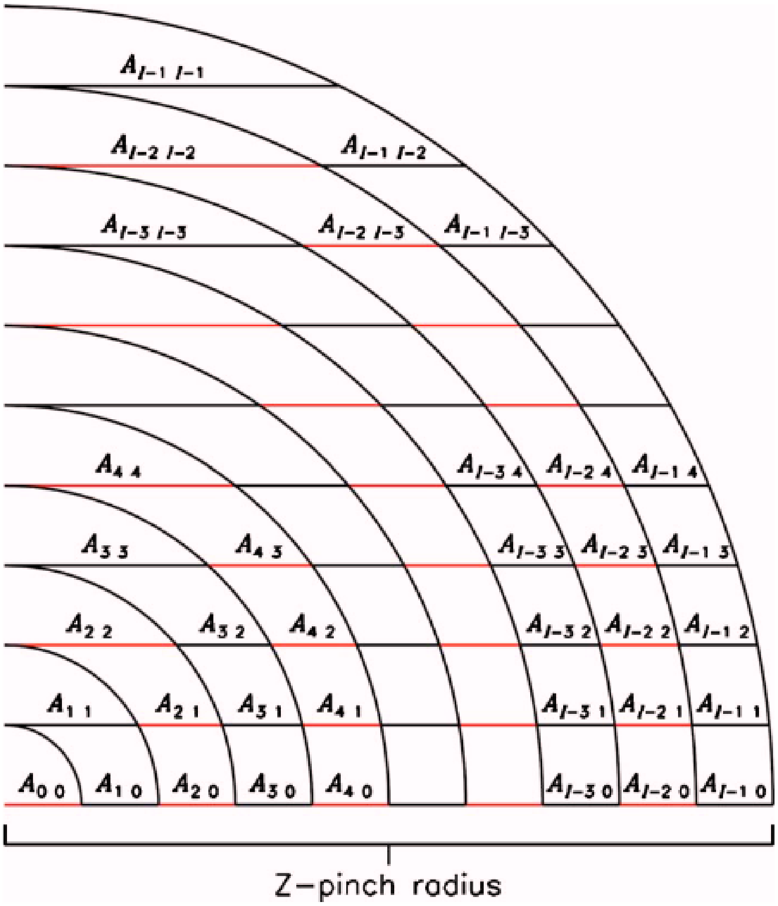

Figure 2.5: A diagram of the lengths used in the length matrix for an Abel inversion [18]. To subtract off the influence of an outer shell from an inner shell, the fitted spectra of the outer shell are weighted by the proportion of the shell passing through the inner chord. The weighted spectra are then subtracted off from the inner shell.

[11]. When subtracting the spectra of the outer shells from the inner shells, the wavelength shift from the instrument astigmatism for that specific viewing chord is used along with the plasma parameters from the outer shells. The rest of the scheme is similar to the Abel inversion: similarity between both deconvolved sides is checked and the assumed geometry of the plasma is readjusted until the calculations for each side converge.

The true plasma temperature is calculated by subtracting the FWHM of the broadened calibration line from the raw FWHM of the plasma line [34].

2.3 Magnetic Field Probes

Magnetic field probes, and specifically b-dot probes, are coils of wire that rely on the principle of magnetic induction to measure the change in magnetic field strength [2]. Faraday's Law for magnetic induction gives the following:

$$\frac{d\boldsymbol{B}}{dt} = \nabla \times \boldsymbol{E} \tag{2.9}$$

Applying Stoke's theorem gives:

$$\oint_C \boldsymbol{E} \cdot d\boldsymbol{l} = -\int_S \dot{\boldsymbol{B}} \cdot d\boldsymbol{s} \tag{2.10}$$

S is the interior area of the coil with circumference C [16]. An integrator is used to convert the rate change of the magnetic field to an absolute magnetic field:

$$V_0 = \frac{NAB}{RC} \tag{2.11}$$

N is the number of turns in the wire, A is the area inside the coil, R and C are the resistance and capacitance of the circuit, and V_0 is the measured voltage [12]. For a plasma confined within a circular geometry, Ampere's law can be used to find the total enclosed current from the b-dot probe:

$$I_{enc} = \frac{2\pi r B}{\mu_0} \tag{2.12}$$

I_{enc} is the current through a circle of radius r.

Azimuthal arrays of b-dot probes can also provide significant insight into the geometry of the magnetic field, and by extension, the plasma. The b-dot probe array data can be decomposed into a Fourier series [12]:

$$B_\theta(\theta_i) = \sum_{j=0,m} a_j \cos(j\theta_i) + \sum_{j=1,m} b_j \sin(j\theta_i) \tag{2.13}$$

The zero ($m = 0$) and first order ($m = 1$) modes are of most significance for this thesis as they provide the strength and center of the magnetic field, respectively [8]. The pinch displacement from the center of the b-dot probe array is:

$$\Delta r = \frac{m_1 r_{wall}}{2m_0} \tag{2.14}$$

r_{wall} is the distance from the center to the b-dot probe array [21].

Chapter 3

EXPERIMENTAL SETUP

3.1 Spectroscopy Setup

The spectroscopy system on ZaP-HD consists of three main components, the telescope and polarization optics, the spectrometer, and the imaging camera system. The optics consist of a 0.5x magnification double telecentric telescope, a two-headed split fiber bundle with ten chords to each head, and polarization optics for resolving the Zeeman split. The telescope was designed by Hartog [14] and is telecentric to ensure that the size of the plasma as viewed from the telescope does not change with distance from the telescope. The telescope is mounted to a carriage which rides on rails above ZaP-HD parallel to the machine's axis to allow for easy adjustments to image different locations along the pinch's axis. Once imaged by the telescope, the plasma emission passes through a quarter-wave plate rotated 45 degrees to the machine axis and a linear polarizer before being imaged by the fiber optic bundle at the telescope's image plane. The heads of the two fiber bundles are stacked on top of one another so each fiber in one fiber head has a corresponding fiber in the other head that it is adjacent to. Figure 2.3 diagrams this polarization setup. The orientation of the linear polarizer is rotated 90 degrees between the two fiber bundles so one fiber bundle only sees the left-hand circularly polarized light while the other bundle only sees the right-hand circularly polarized light. The two fiber bundles combine into a single bundle which feeds into the spectrometer.

The spectrometer is a 0.5 meter Acton SpectraPro Czerny-Turner spectrometer with multiple gratings and an adjustable center wavelength. A 2400 g/mm grating blazed for visible wavelengths was used to provide good resolution of the wavelength shift while also having a high efficiency to ensure good light signal transmission.

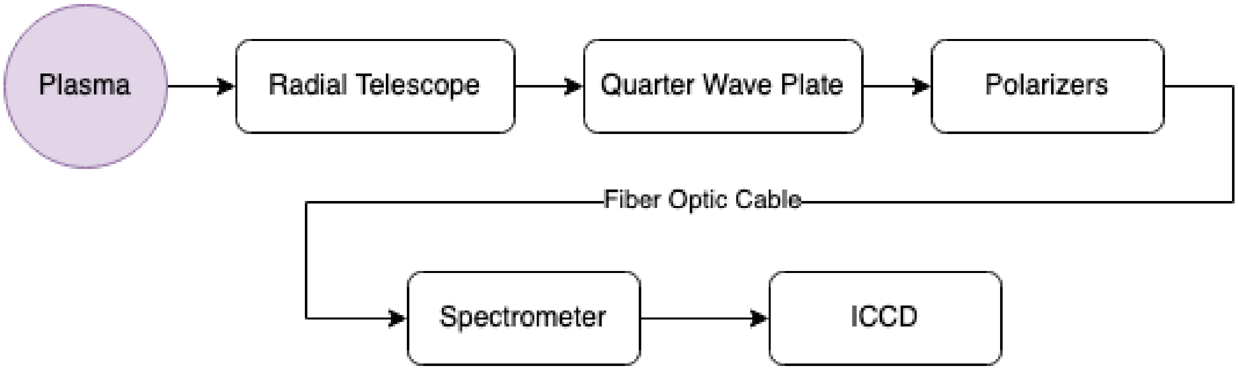

Figure 3.1: Block diagram of the spectroscopy setup with the PI-Max ICCD. The arrows represent the direction of light emitted by the plasma through the system.

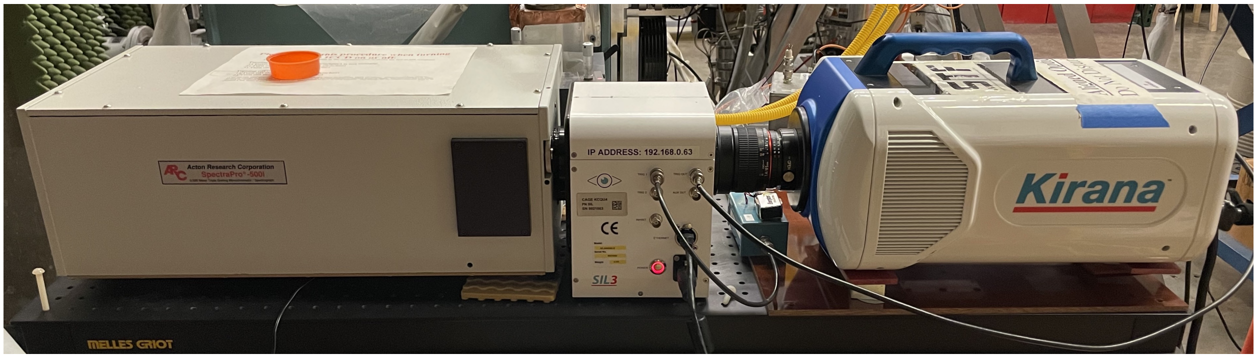

Figure 3.2: Image of the spectrometer, intensifier, and Kirana setup.

Two imaging systems were used for this thesis. A Princeton Instruments Pi-Max ICCD camera was first used to provide single-frame time-resolved measurements. Once these measurements were taken, a Specialized Imaging Kirana-5M was swapped in for the Pi-Max to allow for multi-frame time-resolved measurements. Unlike the ICCD, the Kirana's built-in intensifier cannot amplify the light from the spectrometer enough to be suitably visible. An SIL3 intensifier was placed in between the spectrometer and Kirana to provide significant amplification. Adding the intensifier limits the maximum number of frames to 64 and the usable frame rate to 1M frames-per-second (FPS).

3.1.1 Spectroscopy Calibration

Although already focused by previous experimentalists, the Pi-Max must have its instrument function characterized before being able to provide accurate readings of the plasma. The following process is used: the emission of a specific wavelength of a cadmium pen lamp close to the wavelength being used for plasma measurements is swept across the image sensor by changing the center wavelength on the spectrometer. Gaussian fits of these spectra are used to give precise peak locations and FWHM values. The error between expected peak location and actual peak location is calculated for spectrometer optics correction and the FWHM from each fit is used to calculate an instrument temperature. Once these calculations are made across the x-y image plane of the sensor, quadratic fits that describe the wavelength error and instrument temperature as a function of pixel location are generated. These fits are used during analysis to remove the instrument effects from the raw spectra.

Replacing the Pi-Max with the Kirana and intensifier required both focusing and calibration. Focusing this imaging system is done in two parts. While a mercury pen lamp placed in front of the fiber bundle provides a signal, the intensifier and attached Kirana are aligned and centered in the exit plane of the spectrometer. Once the image is generally in-focus, the lens connecting the Kirana to the intensifier is adjusted until the image appears further in focus. The intensifier and Kirana unit are then adjusted again relative to the spectrometer to further improve alignment and focus. This process is repeated until the spectra viewed by the Kirana is at maximum intensity and minimum broadening. Calibration and determination of the instrument function is performed similarly to the Pi-Max calibration except that multiple frames from the Kirana and averaged together to reduce the image noise.

Wavelength calibration is especially critical as the Kirana software cannot correlate wavelength to pixel location unlike with the Pi-Max. Originally, finding the wavelength per pixel value for the Kirana was done by sweeping the mercury lamp across the image sensor. However, this gave the spectrometer center wavelength as a function of pixel, not wavelength at a fixed spectrometer setting as a function of pixel. Unfortunately, the camera had already

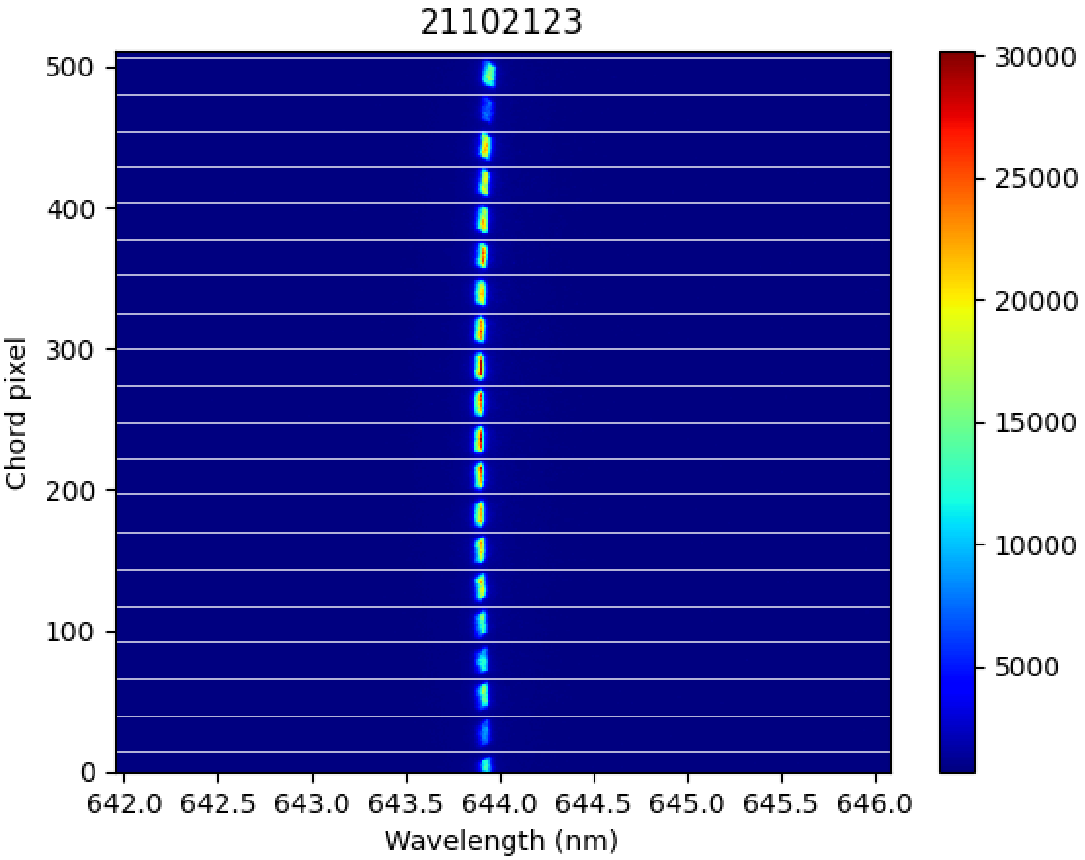

Figure 3.3: A raw ICCD image of the 643.847 nm line from a cadmium calibration lamp. Note the slight curvature of the spectra due to optical effects. This curvature is fit to and subtracted from the spectroscopic measurements.

been removed once this error was realized, but a bootstrapping method was devised where the C IV doublet used for Zeeman splitting measurements was used to determine the wavelength per pixel value. The split in the σ components is symmetrical, so averaging the two σ components gives the center of the original, demagnetized line. Since the wavelengths of the doublet are known, the wavelength per pixel value could easily be found by dividing the difference in wavelength between the two lines by the difference in pixel location between the two lines. The resulting fits for instrument temperature, wavelength error, and wavelength determination are saved and used during analysis.

3.2 Magnetic Field Probes Setup

ZaP-HD contains multiple azimuthal arrays embedded in the outer electrode of the machine to measure plasma current, plasma center, and plasma modes across the assembly region of the pinch. From the nosecone of the inner electrode, arrays of eight equally-spaced azimuthal b-dot probes are spaced every 15 centimeters along the machine's axis. Arrays of four equally-spaced B dot probes are spaced every five centimeters where there is not already a larger array of b-dot probes [23]. During a pulse, the signal from each probe is digitized and recorded to an MDSPlus tree. A Fourier analysis of these data are then conducted to determine modes and location of the pinch at each axial station where there is a b-dot probe array.

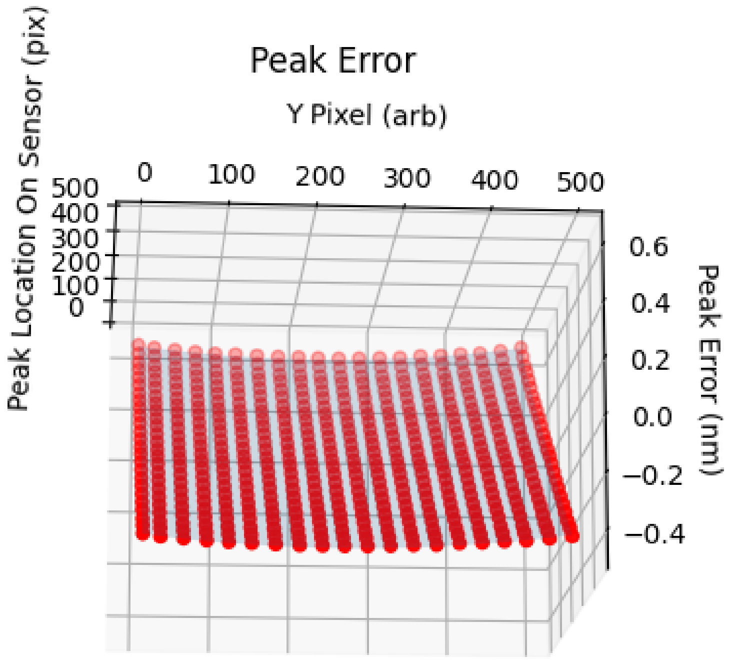

Figure 3.4: Peak errors between the reference wavelength and measured wavelength. Note the parabolic shape along the Y pixel axis due to spectrometer optics. The correction fit is represented by the blue plane.

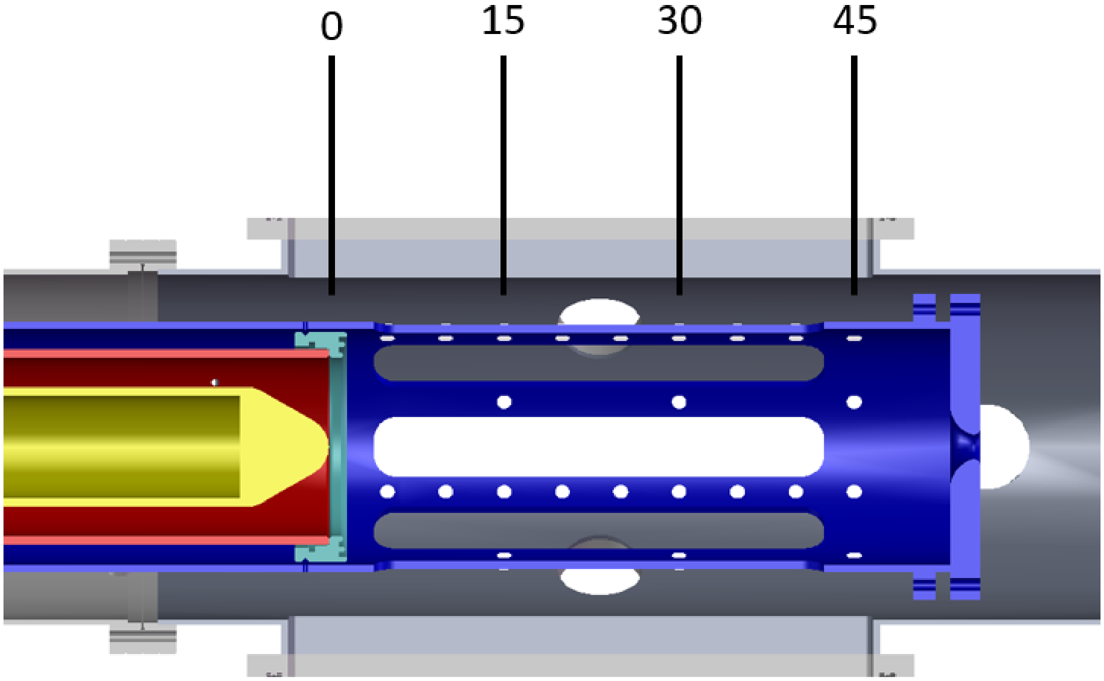

Figure 3.5: Detailed view of the magnetic field probe arrays (white dots against the blue outer electrode) in ZaP-HD. The numbers represent the axial station (in centimeters) of some of the probe arrays [21].

Chapter 4

RESULTS

The C IV doublet at 580.133 nm and 581.198 nm was chosen for this analysis as its ionization energy was high enough to not fully be burned through and the relatively long wavelength of the spectra would increase the apparent Zeeman split. Each line in the doublet was analyzed separately.

4.1 Deconvolved ICCD Measurements

ICCD data was collected at three different periods during the middle (45μs into the pulse), middle-end (60μs into the pulse), and end (75μs into the pulse) of the pinch's quiescent period. The capacitor bank energy was reduced from the maximum allowed bank energy of 9 kV to 7 kV for the acceleration region and from 8 kV to 5 kV for the compression region to ensure the C IV ionization state would be present in significant quantities in the plasma. Even with the decrease in bank energies, signals were still quite weak and a wider gate time for the ICCD was required. The telescope was located approximately 29.5 centimeters from the nosecone.

Wavelength (nm)	State	Orbital	L	J	S	g_j	m
580.133	Ground	$2S$	0	$\frac{1}{2}$	$\frac{1}{2}$	2	$-\frac{1}{2}$
	Excited	$2P^0$	1	$\frac{3}{2}$	$\frac{1}{2}$	$\frac{4}{3}$	$\frac{1}{2}$
581.198	Ground	$2S$	0	$\frac{1}{2}$	$\frac{1}{2}$	2	$-\frac{1}{2}$
	Excited	$2P^0$	1	$\frac{1}{2}$	$\frac{1}{2}$	$\frac{2}{3}$	$\frac{1}{2}$

Table 4.1: Quantum numbers for the 580 nm C IV doublet.

Bank Voltages (kV)	Telescope Loc. (cm)	GPV Timings (ms)	ICCD Gate (μs)
Accel: 7, Comp: 5	29.5	-1.4/-0.8	3

Table 4.2: Table of parameters for ICCD measurements.

A typical current trace of a pulse is shown in Figure 4.1. The spikiness and hash at some points in the trace are due to small disruptions and instabilities in the plasma. The normalized mode data, shown in Figure 4.2, also shows these instabilities, generally defined as when the normalized modes exceed 0.2. Generally, better pinch stability is achieved with higher bank voltages as the increased energy results in higher axial plasma flow rates which leads to increased shear and stability. With the threat of burn-through of the C IV line, bank voltages were kept lower and resulted in weaker, less stable pinches.

4.1.1 Middle ($T = 45\mu$s) Quiescent Period Measurements

Although the quiescent period begins around 20-25 μs into the pulse, strong signals were generally not seen until later in time as plasma flowed past the axial location of the telescope. As a result, ICCD measurements were taken around or after total peak current. However, while measurements taken at $T = 45\mu$s were taken at or past the total peak current, the localized current near the axial location of the telescope at P29 was only approaching or just at maximum current (Figure 4.3).

Raw spectra taken during this time were deconvolved using the method described in section 2.2. Ion temperatures were then determined from the instrument broadened Gaussian using Eq. 2.8. Carbon ion temperatures were generally between 20 and 40 eV, corrected for instrument temperature. Temperature agreement was especially good between the "top" and "bottom" chords (each of the two stacked fiber bundles) as well as between the carbon doublet lines, suggesting consistent measurements. Furthermore, temperature profiles were mirrored across the determined center of the pinch. These mirrored profiles indicate suc-

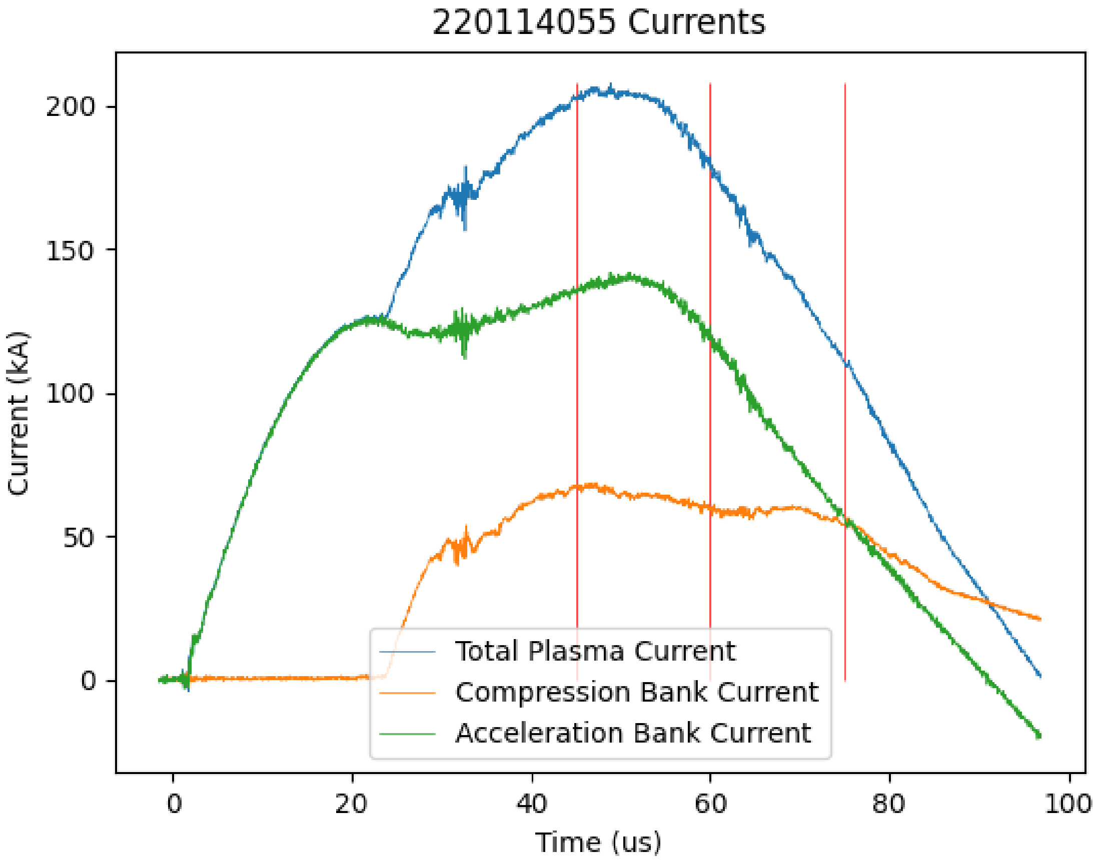

Figure 4.1: A typical current trace for ZaP-HD. The red, vertical lines mark where ICCD data was taken (45, 60, 75 μs). The total plasma current is the sum of the acceleration and compression currents.

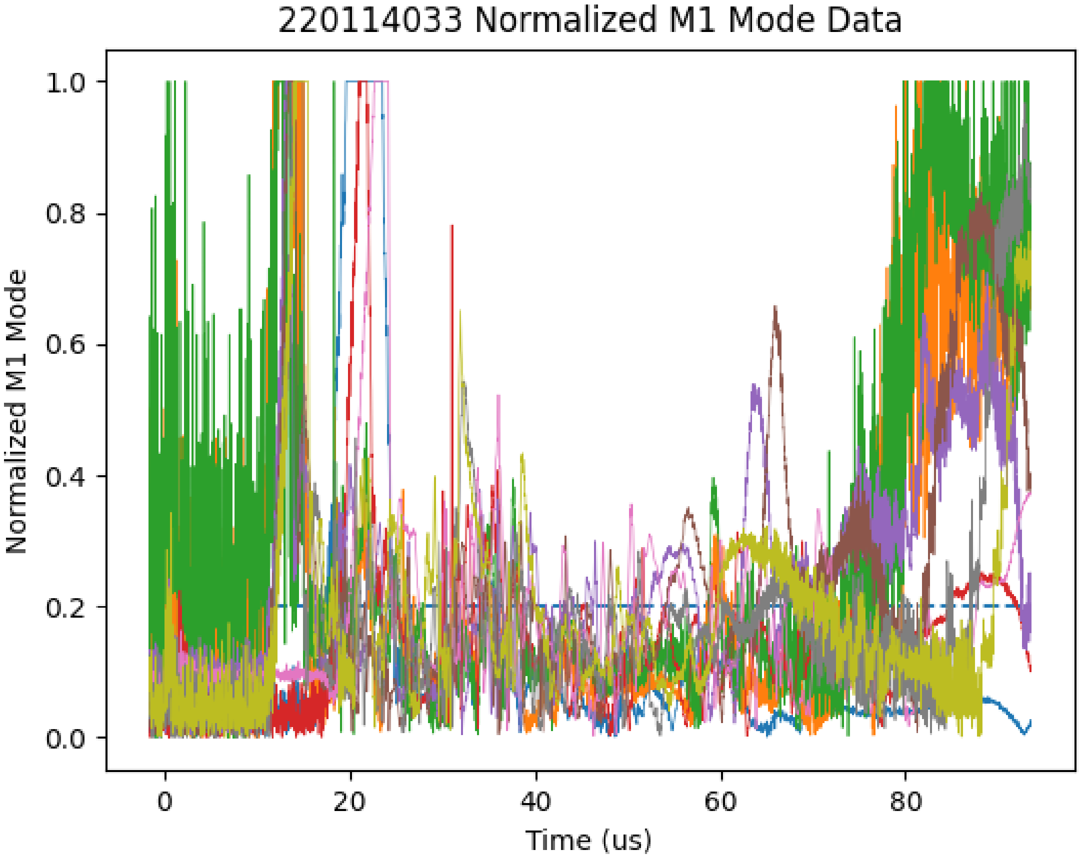

Figure 4.2: Normalized magnetic field mode data. Quiescence is empirically achieved when all the normalized magnetic modes are at or below 0.2 (dashed, horizontal line). Quiescence was significantly harder to achieve for these low power pulses.

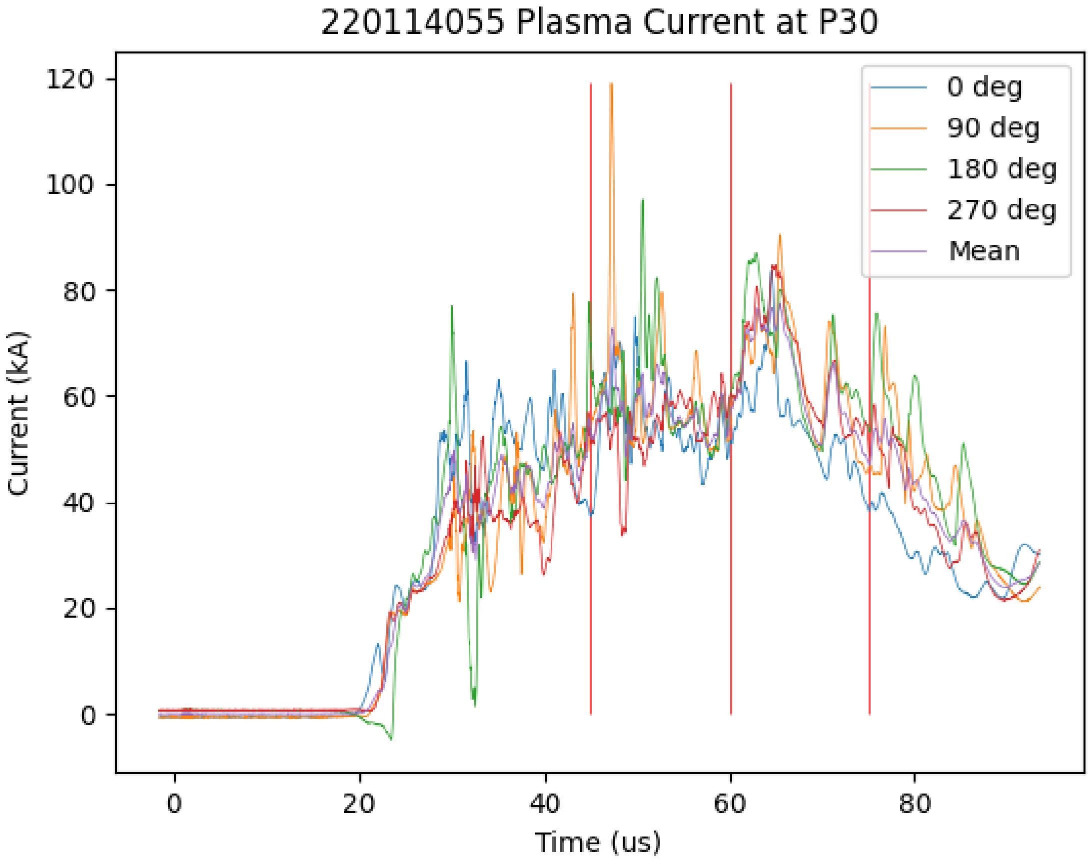

Figure 4.3: Plasma current at P30 as seen by the magnetic field probes. Note that total plasma current peaks before the P30 plasma current peaks. The red, vertical lines mark where ICCD data was taken (45, 60, 75 μs).

cessful deconvolution as each plasma shell should have very similar temperatures across the axis. The temperatures being lower near the center of the pinch also shows that artificial broadening from the outer shells has successfully been removed. Convergence of these mirrored profiles also confirms, while not unexpected, that the plasma is collimated with axial symmetry.

Wavelength shift of the centroids of each spectra due to Zeeman split where also found with the same deconvolution scheme used to find ion temperatures. These wavelength shifts were then used to compute magnetic field strength using the small field Zeeman splitting approximation shown in Eqs. 2.2 and 2.3. Since Zeeman splitting is incredibly sensitive to wavelength shift of the σ components, resolving intuitive magnetic field measurements was quite challenging. Conceptually, the field null should be at the center of the pinch which, as determined earlier by deconvolution, is near the center of the machine axis. Since deconvolution also assumes that the shells of constant plasma parameters are concentric, the magnitudes of the magnetic field across the field null should be equal. The magnetic field generally follows these assumptions with a field null near the center and symmetric magnetic field magnitudes across the center as radius increases. By Ampere's Law (Eq. 2.12), the magnetic field at a certain radius is proportional to the enclosed current. As the radius of the Amperian loop decreases, the magnetic field should also decrease towards zero, and does.

The edge of the pinch can be found where the magnetic field goes to zero, as there should be little to no ion density at the edge of the pinch. Figure 4.5 gives a pinch radius of approximately 10-12 mm. This result is interesting as it gives a radius of the pinch that does not match the edge of the pinch as determined by deconvolution (the edge of the emission). Figure 4.4 shows very little temperature difference across the magnetized edge of the plasma.

Further insight can be gleaned by examining the current density. Applying Ampere's law without the displacement current (Eq. 1.2) gives the current density, shown in Figure 4.6. Since this calculation takes the derivative of an already sensitive measurement, conclusions from these current density calculations should be taken with care. Intuitively, current should be where the pinch is, and in this case, it generally is. High current densities on the order

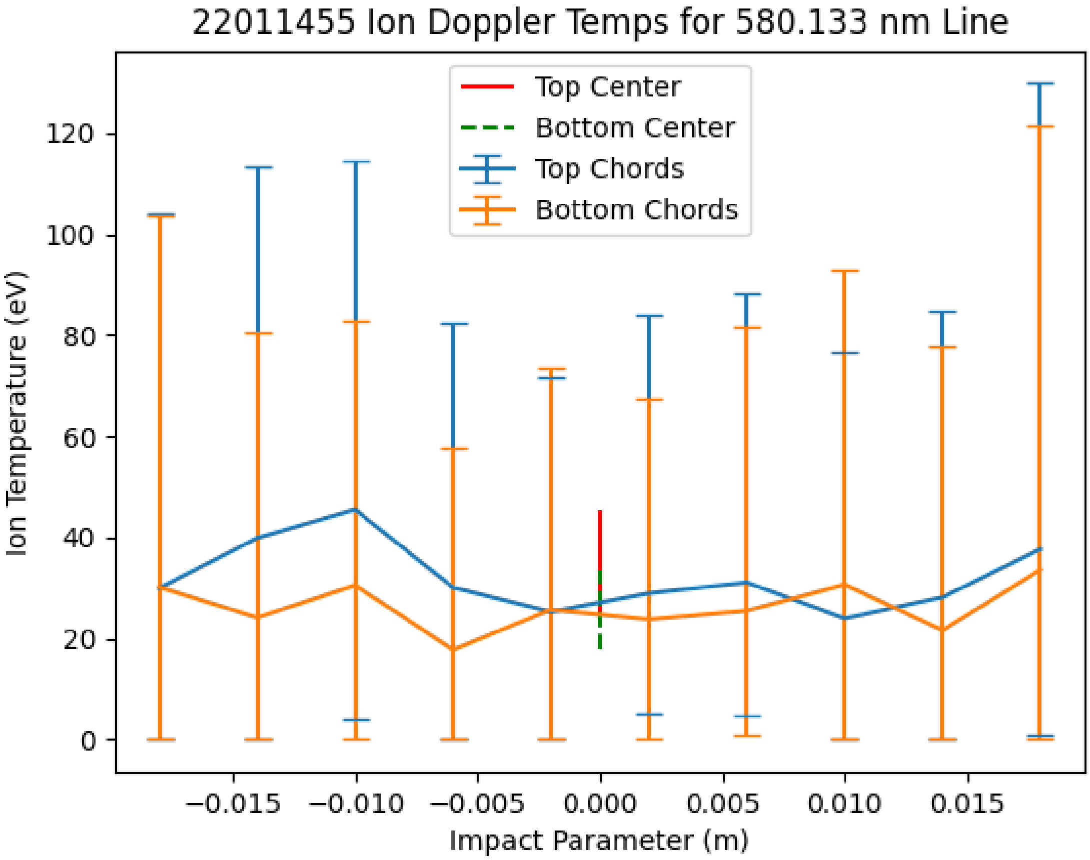

Figure 4.4: Deconvolved C IV impurity ion temperatures at $T = 45\mu$s. Note excellent temperature agreement between the two chord bundles as well as spatial agreement for pinch center and pinch edge.

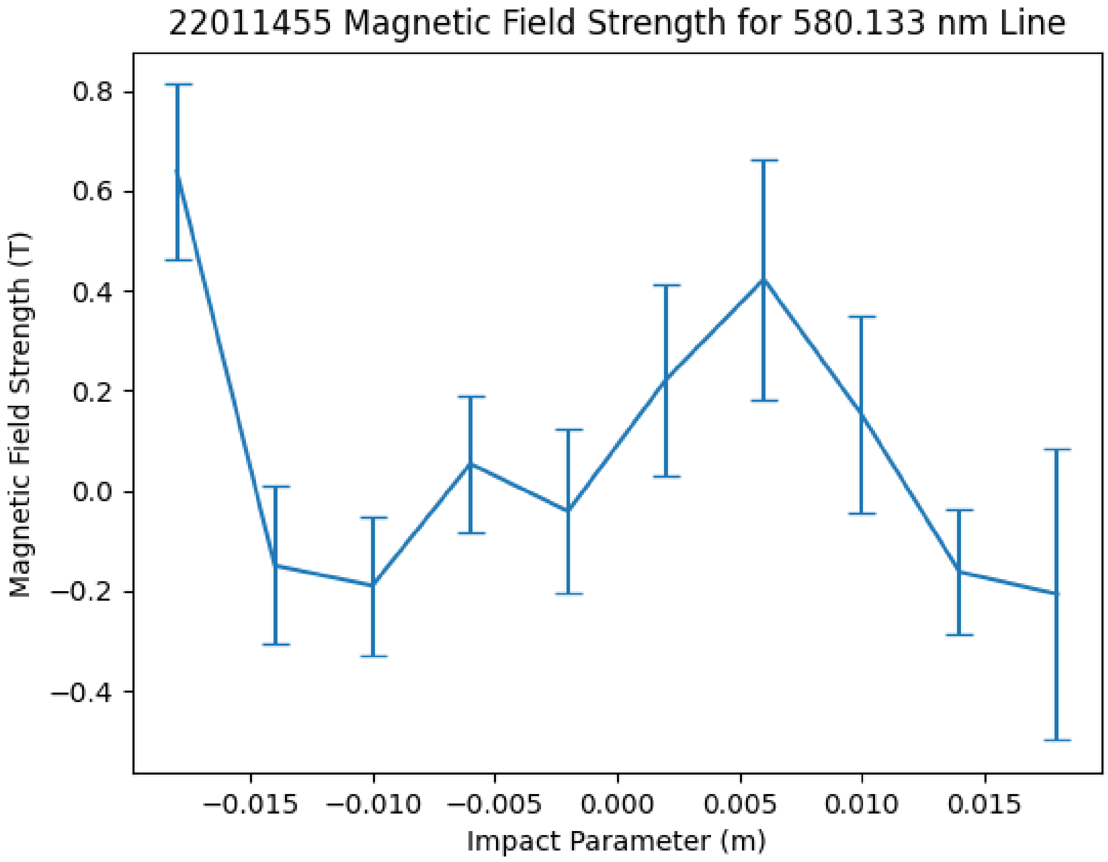

Figure 4.5: Deconvolved magnetic field strength at $T = 45\mu$s. A field null is visible and expected at the center of the pinch (impact parameter = 0 m). The magnetic field grows roughly linearly from the center. Since the magnetic field rotates around the field null, the sign of the magnetic field strength should change across the axis, and does, since the magnetic field is in the opposite direction once across the field null. The location of the maximum magnitude of the magnetic field indicates the edge of the plasma. At the edge of the plasma, the magnetic field should fall off with 1/r. This trend is not observed. The most likely cause for this discrepancy is due to instrument effects and a weaker signal that is harder to resolve well at the edge of the sensor.

of $50\frac{\mathrm{A}}{\mathrm{mm}^2}$ exist near the core of the pinch and drop off rapidly to approximately zero around 3-4 mm from the pinch center. There is only pinch current in the core of the pinch, although the emission extends further out into the outer shell. Since current is the relative motion between ions and electrons, the outer shell having no current suggests that the outer region, although an excited, line-emitting plasma, does not have any current. This kind of plasma, where the net current is zero, can be created in the acceleration region since the $\boldsymbol{J} \times \boldsymbol{B}$ force accelerates both ions and electrons in the same direction. This outer shell of the pinch, where current is zero, is the plasma that provides shear-flow-stabilization to the inner core of the pinch.

Another interesting aspect of the current profile is the current dropping to zero near the pinch axis, suggesting that more of the current could be flowing through the outer shell of the pinch. Unfortunately, no other shots saw a similar trend so no conclusions can be made yet. However, this phenomenon does warrant further investigation.

4.1.2 Late ($T = 60\mu$s) Quiescent Period Measurements

Many similarities in plasma parameters were apparent between the two measurements at $T = 45\mu$s and $T = 60\mu$s. Generally, ion temperatures were uniform across the pinch and around the same 20 - 40 eV temperature range as measurements taken 15μs earlier. At the edge of the viewing chords, temperatures where higher, even after correcting for the increased broadening towards the edge of the spectrometer. A weak spectroscopy signal could give an artificially broadened temperature since the reduced signal-to-noise ratio makes fitting to the true signal without including noise more difficult. The b-dot probe current trace shows the plasma reaching peak current around this time period. Assuming that ohmic heating is the dominant heating process, the ion temperature should be higher with increased current, but that is not the case. Shot-to-shot variability was generally quite high. Figure 4.7 shows temperatures taken at 60μs that were at similar or lower temperatures than for the temperatures found 15μs earlier in the pinch life.

Zeeman splitting measurements at this time in the pinch life showed a weaker magnetic

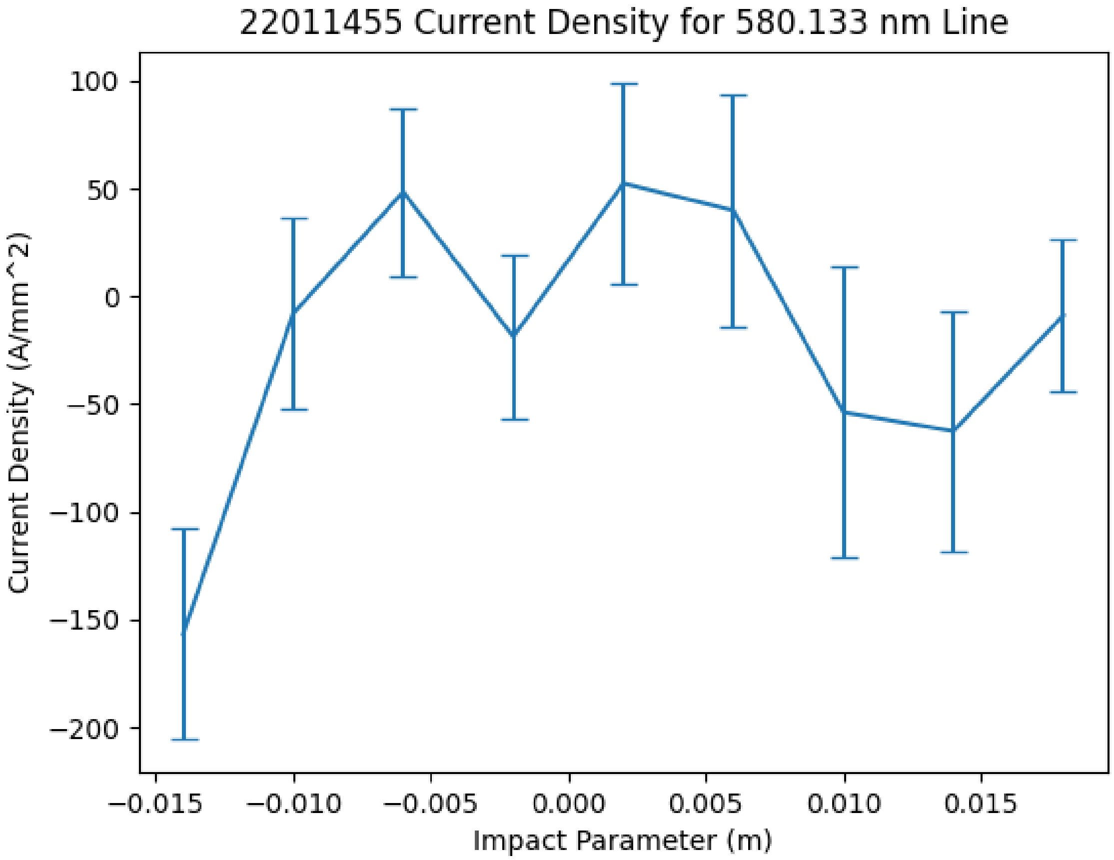

Figure 4.6: Deconvolved current density at $T = 45\mu$s. The current is somewhat uniform across the pinch, with an interesting drop to zero near the pinch center. Although this drop is not seen in any other current density measurements, it may warrant further investigation. This measurement is especially sensitive as it is the derivative of the already sensitive magnetic field measurements. As a result, the current density measurements at the edge of the pinch where the signal is weaker give particularly nonsensical results.

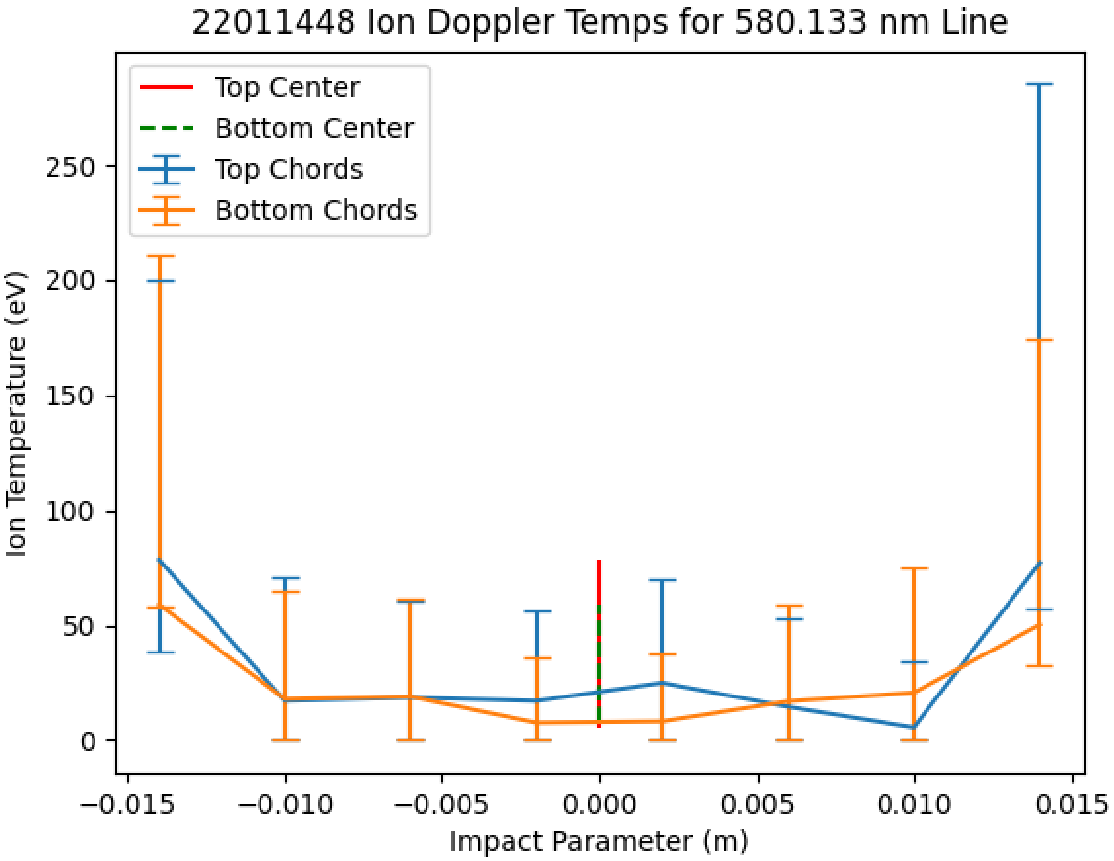

Figure 4.7: Deconvolved C IV impurity ion temperatures at $T = 60\mu$s. The temperatures for this pulse were lower than for other pulses at the same time by around 10 eV. This speaks to the shot-to-shot variability that can make understanding the evolution of the pinch without a multi-frame imaging system challenging. The anomalously high temperatures at the edge of the viewing window are due to the very weak signals seen at the edge of the image sensor. Instrument noise artificially broadens weaker signals and gives artifitially higher temperatures for weaker signals.

field (Figure 4.8), with a maximum field strength around half of the field strength seen 15μs earlier. The radial extent of the magnetic field is also slightly smaller than the magnetic field from the earlier time period. The calculated current density profile matches this slightly smaller pinch core. Although the pinch core is smaller and the ion temperatures at the core are higher, compression heating is most likely not a factor here. For compression heating to be at play, the magnetic field would have needed to be higher to handle the increased plasma pressure, according to the force balance described in Eq. 1.3. The opposite is true: the magnetic field is weaker and therefore confinement is weaker too.

4.1.3 End of the ($T = 75\mu$s) Quiescent Period Measurements

At the end of the quiescent period, ion temperatures where generally lower by 10-30 eV than during the quiescent period. These results make sense as mode data shows that the pinch falls apart and begins dissipating at the end of the quiescent period. The plasma cools as it disperses outward, and ion temperatures decrease further.

Collapse of the pinch is also confirmed by Zeeman splitting measurements. Figure 4.11 shows that the magnetic field has dropped close to zero. Confinement of the plasma is no longer possible and the plasma disperses. Current density measurements (Figure 4.12) also confirm the pinch collapse as very little appreciable current is in view.

4.2 Kirana Measurements

Since the Kirana intensifier is limited to 64 frames at a frame rate of 1M FPS, determining the start of an appreciable spectroscopic signal is critical. Generally, emissions became visible around $25-35\mu$s and lasted until around 80μs, primarily limited by the maximum 64 intensified frames of the intensifier. The slightly decreased exposure time to allow for the high frame rate and intensifier phosphor decay time compared to the ICCD resulted in dimmer spectra. These weaker signals make analysis more difficult, especially when subtractions need to occur for deconvolution. However, Kirana measurements were taken at P10, where pinch emissions are brighter to help offset the reduced signal. The capacitor bank voltages

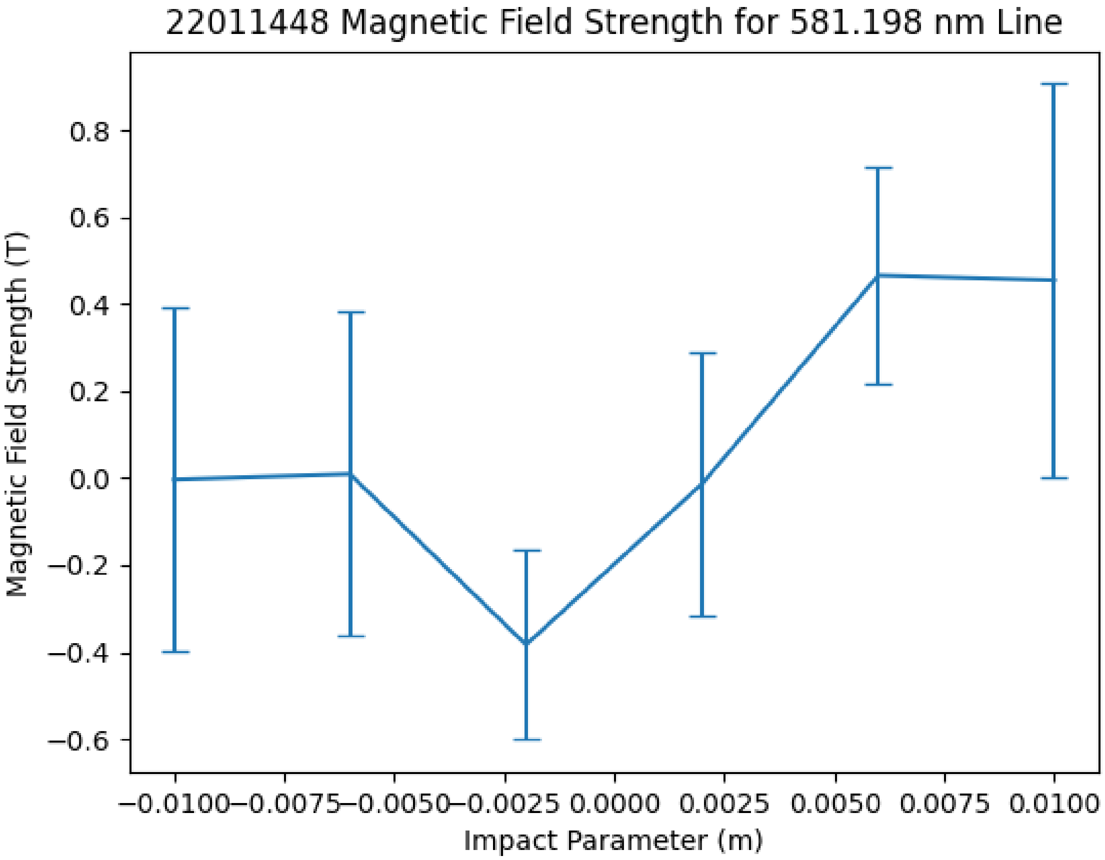

Figure 4.8: Deconvolved magnetic field measurements at $T = 60\mu$s. The field null is roughly at the pinch center as expected. The trend of linearly increasing magnetic field magnitude away from the center of the pinch is once again observed like in figure 4.5. Similarly, the 1/r drop off at the edge of the pinch is still not seen likely due to the weak signal at the edge of the spectrometer.

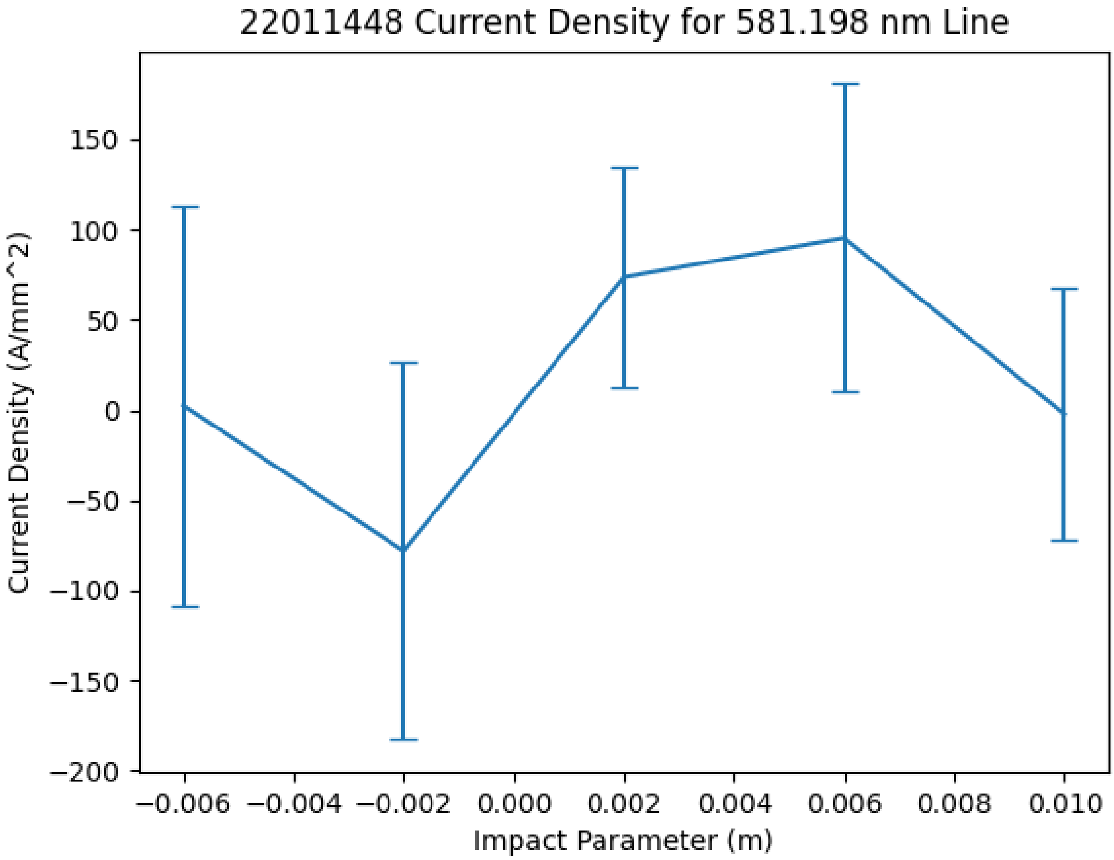

Figure 4.9: Deconvolved current density at $T = 60\mu$s. The lack of resolvable measurements makes drawing significant conclusions difficult. However, as expected, the magnetic field edge defines the current density edge. The current densities are also of similar magnitude to currents seen earlier in the pinch life (figure 4.6)

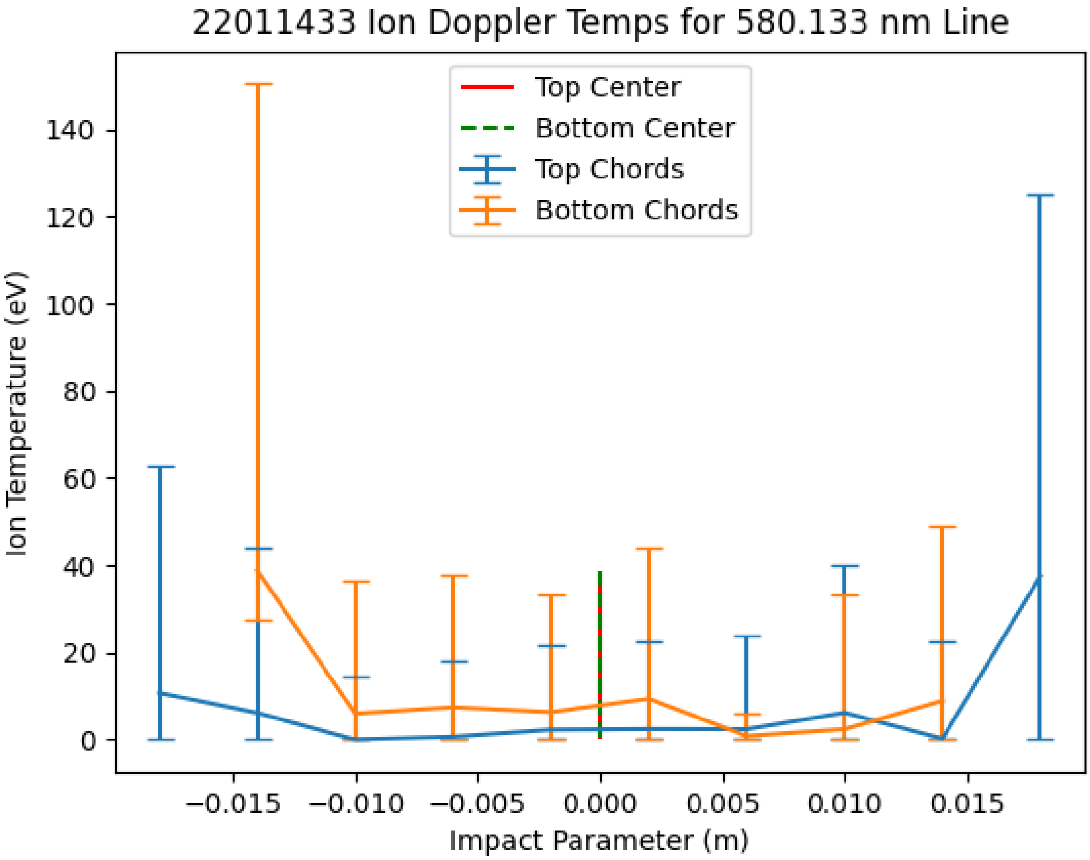

Figure 4.10: Deconvolved C IV impurity ion temperatures at $T = 75\mu$s. The end of the pinch's quiescent period is readily apparent by the dramatic drop in temperature compared to earlier in the quiescent period. This suggests that the end of the pinch confinement results in rapid cooling of the plasma through the lack of heating and plasma dissipation.

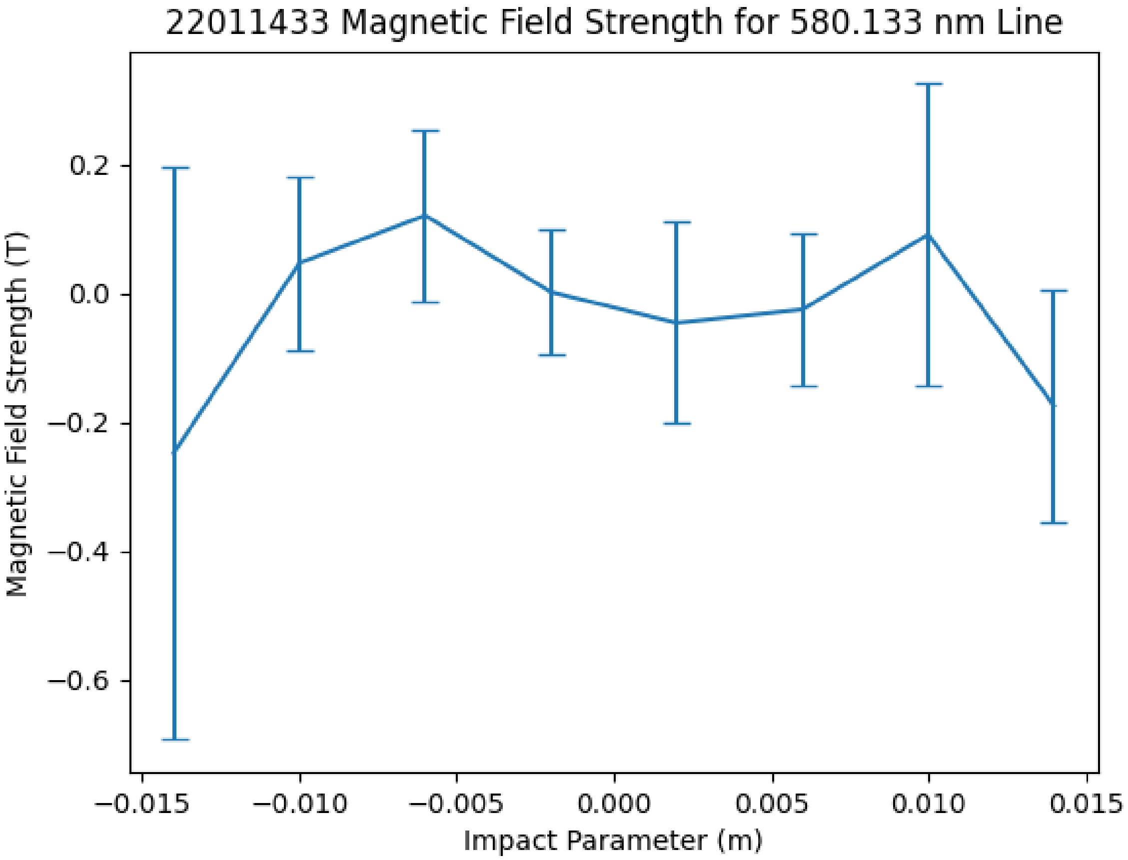

Figure 4.11: Deconvolved magnetic field measurements at $T = 75\mu$s. The lack of appreciable magnetic field indicates the end of the pinch confinement and the end of the pinch itself. The measurements past the 0.01 m impact parameter are once again anomalous due to weak signals or poorly captured instrument effects.

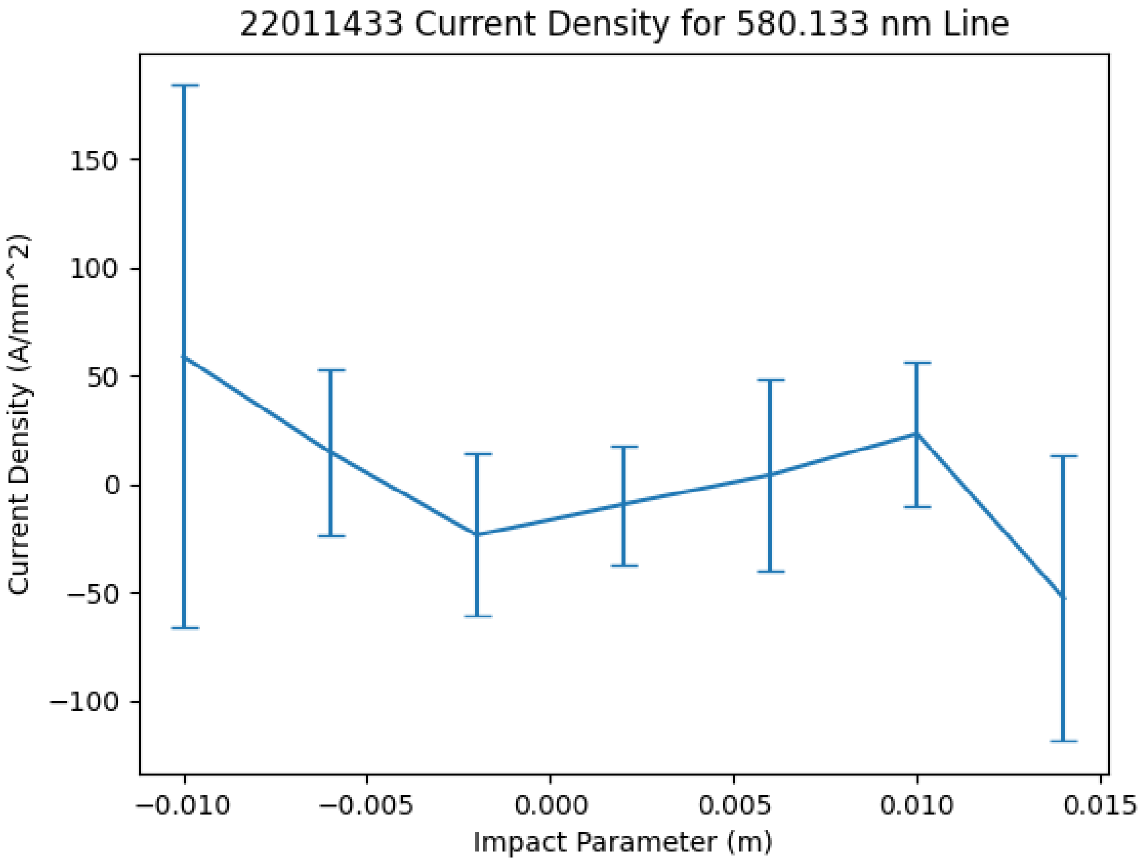

Figure 4.12: Deconvolved current density at $T = 75\mu$s. The lack of appreciable current density indicates the end of the pinch.

for these shots were the same as used for the ICCD measurements.

Although the raw Kirana data appeared strong enough to be easily resolved, analysis of the data showed that the signals were quite weak and difficult to fully resolve. Figure 4.13 shows the resolvable temperature plots.

Kirana temperatures and ICCD temperatures were quite similar, with peak temperatures at 60μs when the peak current occurred. The temperature agreement is quite interesting as the measurements where taken at axial locations 20 centimeters apart. There is significant disagreement with temperature measurements taken by Forbes using the Kirana. Forbes saw measured ion temperatures increasing significantly later in the pulse [7]. Similar trends were confirmed in this work for the uncorrected temperatures. However, once temperatures were corrected for instrument broadening, the temperature trends agreed closely with ICCD measurements. The anomalous temperatures could be due to artificial broadening from noise, similarly to how the temperatures near the edge of the camera sensor are higher. After the quiescent period, emissions should significantly decrease as the plasma begins dispersing. The weaker emission signals result in a higher signal-to-noise ratio, allowing noise to broaden the plasma since the signal is harder to distinguish from the background noise.

Since magnetic field measurements require good resolution of the line centers for both pairs of the fiber optic bundle, any inability to resolve one half of the pair will make resolving the Zeeman split and magnetic field for that pair impossible. Figure 4.14 shows the few resolved magnetic field measurements taken by the Kirana. Generally, the magnetic field magnitudes match the ICCD measurements, with magnitudes around a quarter of a tesla a short distance away from the field null. Although fields were small and tended towards zero at the end of the quiescent period, the errors were quite large, the weak signal the most likely cause. As the signal grows weaker towards the end of the pulse, the signal-to-noise ratio decreases, reducing the goodness of the fit and increasing the error.

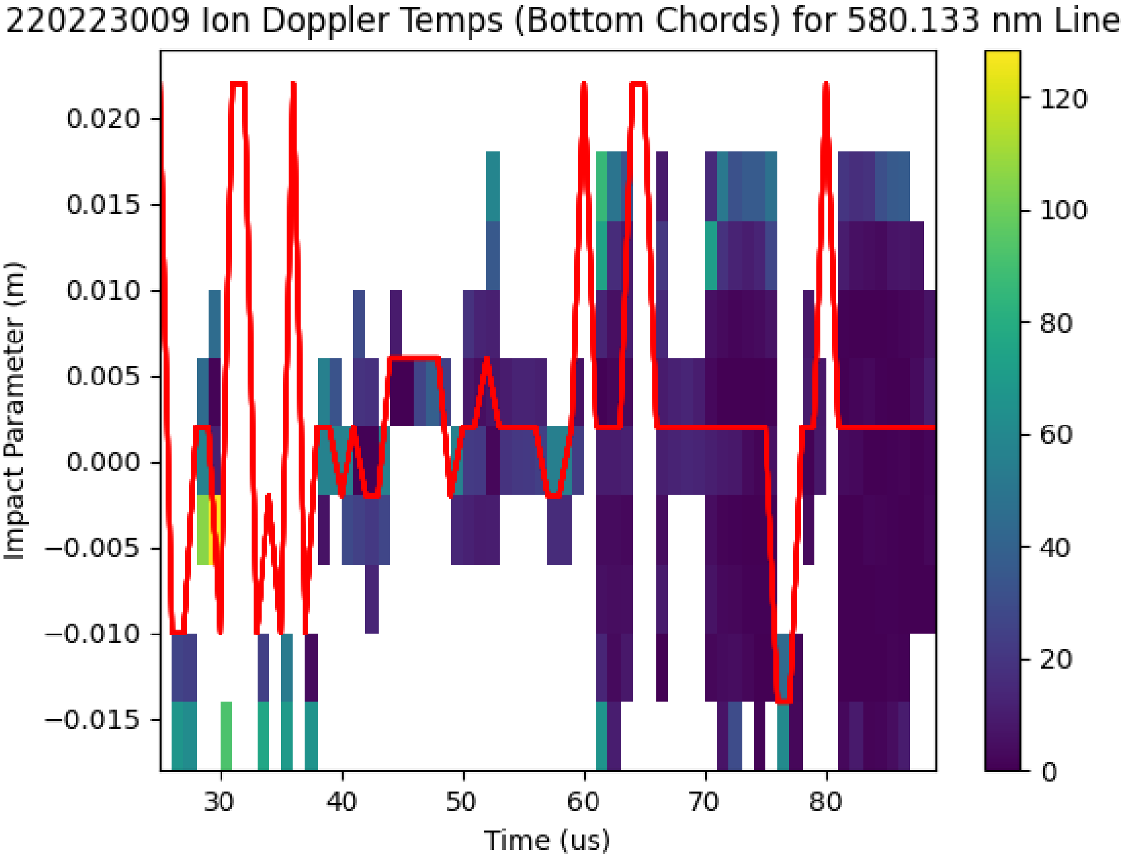

Figure 4.13: Deconvolved ion Doppler temperatures as recorded by the Kirana. The red line denotes the pinch center as determined by deconvolution. General temperature agreement between the Kirana and ICCD measurements is seen with temperatures in the pinch center on the order of 20-40 eV. The temperature evolution over time is also clearly visible with higher temperatures near times of high current during the quiescent period.

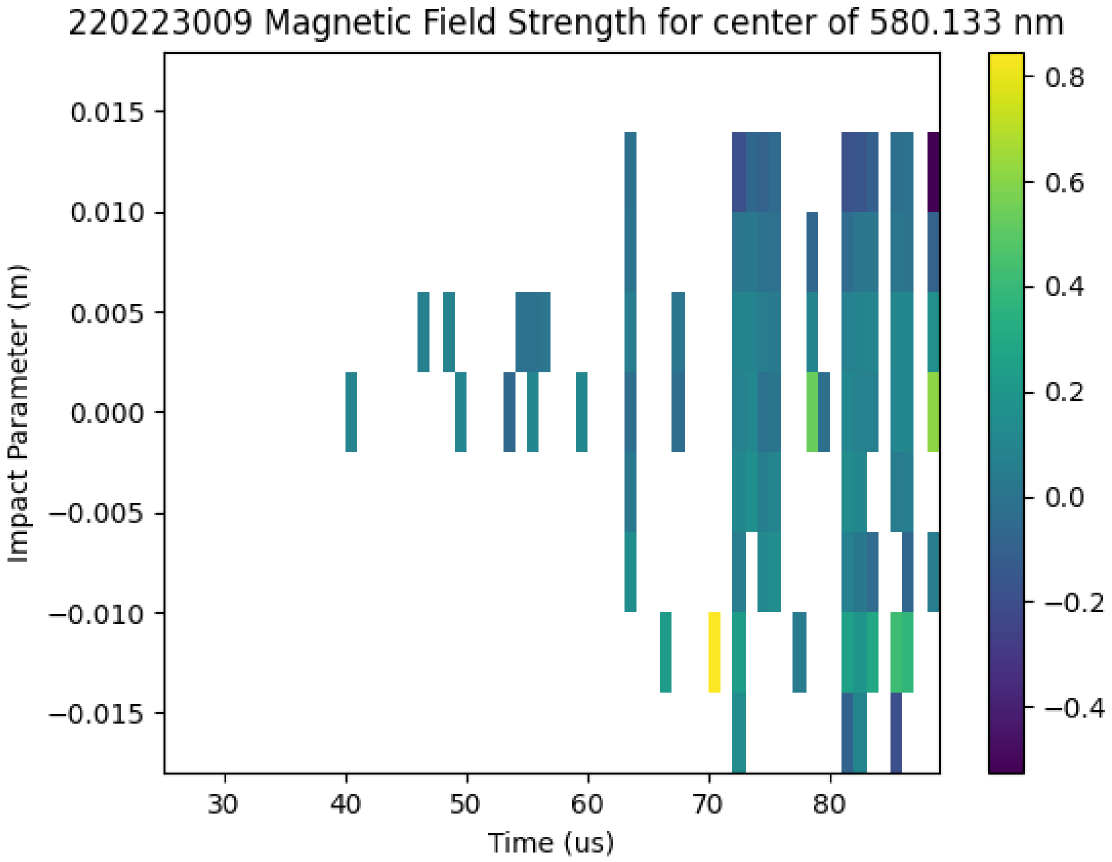

Figure 4.14: Sparse Zeeman splitting measurements taken by the Kirana. The magnitudes of the magnetic field agree with the magnitudes seen by the ICCD. The magnetic field measurements are more sparse due to the need to successfully resolve parameters for both the top and bottom chords. If one of the spectra in the pair is not successfully found, the Zeeman split cannot be determined. The sparseness of these data make drawing any specific conclusions difficult and motivate another run campaign with more optimized camera settings for successfully resolving more of the spectra.

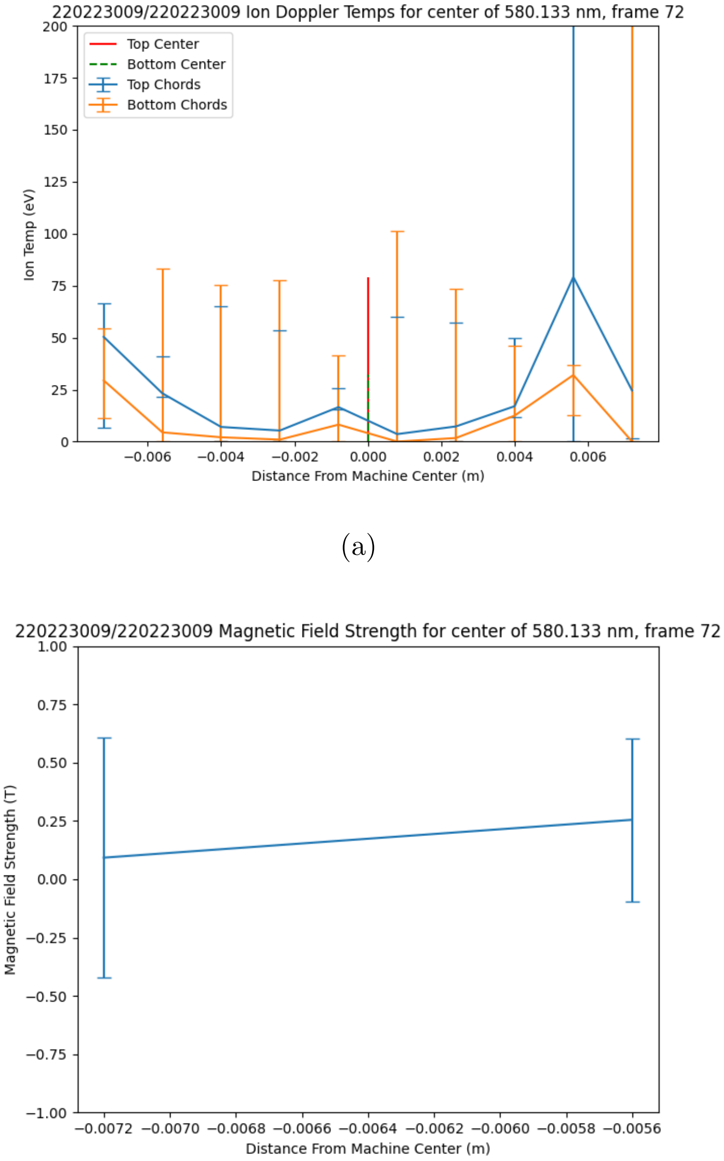

(a)

(b)

Figure 4.15: Deconvolved (a) temperature and (b) magnetic field strength during a single frame near the end of the quiescent period. The large error bars are due to weaker, harder to resolve spectra compared to the strong signals measured by the more-optimized ICCD settings.

4.3 Comparison With B-Dot Probe Measurements

For ICCD measurements, the radial telescope was located about 0.5 centimeters in front of the P30 b-dot probe array. Since this distance is small, the P30 b-dot probe measurements were compared directly with the ICCD results. For Kirana measurements, data was taken at P10.

4.3.1 Pinch Center Comparisons

Both the ICCD and Kirana spectroscopy measurements give the center of the plasma by radial deconvolution. Those centers can then be directly compared to the pinch center found by the b-dot probes. Critically, while the pinch center found through deconvolution uses the ion temperatures to measure convergence and ultimately find the center of the pinch, the b-dot probes use the magnetic field strength, which is a function of current, to find the pinch center. Although the deconvolution scheme assumes that plasma parameters in each "shell" are the same, the pinch center is still being found with very different plasma parameters.

Table 4.3 lists the locations of the pinch centers from characteristic individual shots as determined by the ICCD and by the b-dot probes. ICCD pinch center results show slight agreement with the pinch center as determined by the b-dot probes. The maximum difference seen is just over a centimeter, but the lack of change in the ICCD determined pinch center to match the change in the b-dot determined pinch center over the life of the pinch suggests that the two measurements are not well correlated. The most likely reason for the lack of agreement the long gate time needed by the ICCD to capture a strong signal. The 3μs gate time of the ICCD gives significant time for the pinch to wiggle around. Instead of determining the true center at the opening of the gate, deconvolution will instead determine a time-averaged center over the time that the gate is open. Figure 4.16 gives a perfect illustration of how the rapid movement of the pinch can greatly impact the deconvolution determined pinch center. For the specific pulse in figure 4.16, the ICCD was triggered at 45μs, precisely when a large shift in the pinch center occurred. Over the time that the gate

Time (μs)	45	60	70
ICCD Pinch Center (mm)	0	0.4	0
B-dot Pinch Center (mm)	10.6	2.2	1.4
Difference (mm)	10.6	1.8	1.4

Table 4.3: Table of comparison of pinch centers as determined by deconvolved ICCD measurements and b-dot probe measurements. The ICCD pinch centers where the average of the centers for each line in the C IV doublet.

was open, the pinch moved by almost two centimeters with an average location near the center of the machine axis. Deconvolution successfully captured the average center over the exposure period, but the long exposure period meant that deconvolution could not capture the true center of the pinch at exactly 45μs.

Comparisons in pinch center between the b-dot probe array and Kirana were also made and are shown in Figure 4.17. Although both center calculations deviate from the center at somewhat similar times, very little correlation can be made between the two pinch center calculations. In general, the spectroscopy-calculated center stayed near the machine axis while the b-dot array-calculated center strayed further from the machine axis. A possible reason for the different locations could be noise from the b-dot array influencing the center location. Since the plasma movement inside ZaP-HD is both transient and turbulent, the more random and dynamic movement of the plasma can be easily picked up by the probes. The center of the plasma at some points, according to the b-dot probes, is completely out of the approximately one centimeter viewing radius of the spectroscopy optics. If the center of the plasma is out of view of the imaging optics, deconvolution cannot work since the plasma center must be able to be determined for the algorithm to converge. These large pinch shifts could help explain the sparse results from the camera. Near the end of the pinch quiescent period, deconvolution predicts a centered pinch while the b-dot probes show fluctuations on

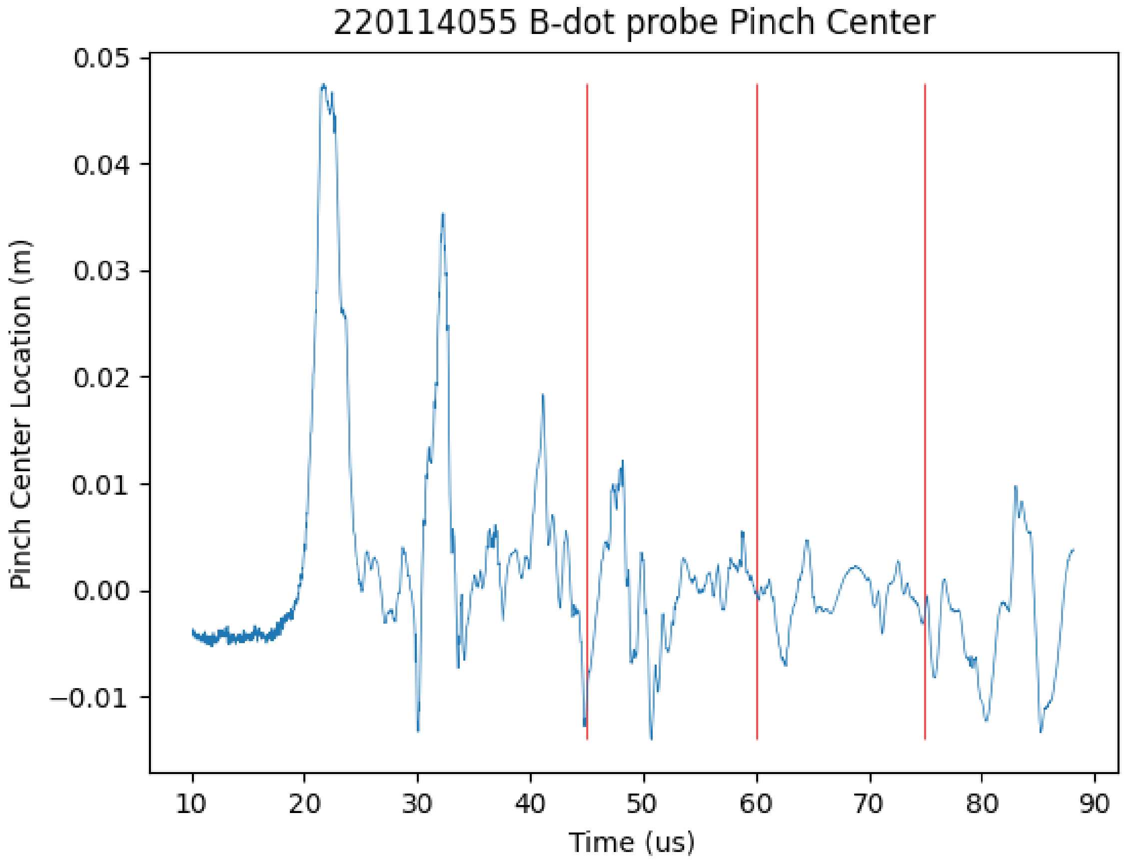

Figure 4.16: A b-dot probe pinch center location trace. For this pulse, the ICCD was triggered at 45μs (first vertical red line). A large shift in pinch center occurs during the 3μs period the ICCD gate is open. As a result, deconvolution determined a pinch center near the center impact parameter, which was approximately the average location of the pinch center over the exposure period of the ICCD.

Time (μs)	45	60	75
ICCD Pinch Current (kA)	12	35	20
B-dot Pinch Current (kA)	53	82	52
Difference (kA)	41	47	32

Table 4.4: Table of comparison of pinch currents at P30 as determined by deconvolved ICCD measurements and b-dot probe measurements.

the order of one centimeter from the machine center. The low plasma temperatures at the end of the pinch life are the most likely culprit. Deconvolution requires that a small temperature error between the pinch-center determined temperatures be allowed to ensure convergence. When the plasma temperatures are already low, the allowed temperature error between the two chords becomes relatively large, allowing deconvolution to converge at many possible locations since the temperatures do not change greatly across various impact parameters.

4.3.2 Magnetic Field Comparisons

ZaP-HD's magnetic field probes and Zeeman splitting spectroscopy provide two ways of measuring the pinch's magnetic field, and by extension, the pinch current at various axial locations along the machine. Total (enclosed) pinch current at a specific axial location was found by using Eq. 2.12. For the b-dot probes, the radius for the Amperian loop enclosing the current was radius of the inner face of the inner electrode, about 10 centimeters. For the spectroscopy diagnostics, the maximum radius of the Amperian loop was determined by the largest radius where magnetic field could still be measured.

The b-dot probes measured significantly greater current than the spectroscopy diagnostic. Figure 4.19 provides a clear example of the significant discrepancy in measured magnetic field strength, used to calculate pinch current, between Zeeman splitting and the b-dot probes. Since the entire radial extent of the pinch is captured by the spectroscopy system,

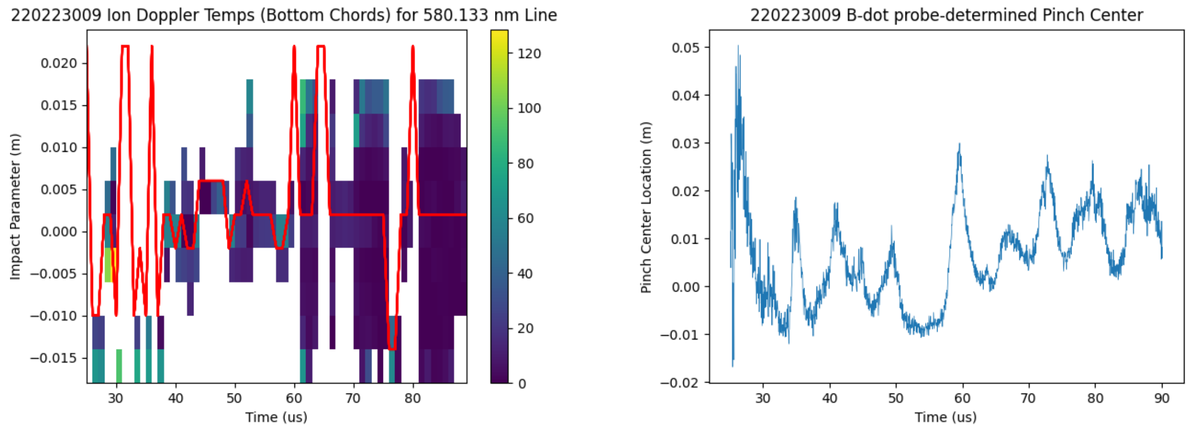

(a)

(b)

Figure 4.17: A comparison of (a.) Kirana temperatures and pinch center location (red line) to (b) pinch center location as determined by the b-dot probes. Fluctuations in the pinch center are seen to occur at similar times by the two diagnostics. Deconvolution cannot successfully resolve spectra where large fluctuations occur since the pinch can travel out of viewing range. The fluctuation near 60μs is a good example of a large fluctuation outside the viewing range of the spectroscopy system. At 60μs, the deconvolution scheme cannot resolve the pinch center as the pinch center is completely out of view. Deconvolution tends to predict a more-centered pinch compared to the b-dot probes, especially later in the pulse. This is due to the small pinch-center temperature errors needed to allow deconvolution convergence. Since temperatures are very low relative to the allowed convergence error at the end of the pinch life, deconvolution can easily converge in many locations with the wrong geometry. In this case, deconvolution keeps the pinch center near the 0 impact parameter when the pinch center should be displaced from the machine center to match the b-dot probes.

all of the pinch current is in view of the radial telescope. Therefore, the Zeeman splitting measurements should be able to capture all of the pinch current. The large propagated errors of the magnetic field measurements could close some, but not all of the current deficit. The most likely cause for the current difference is the extended gate time needed by the ICCD to capture a strong signal. The b-dot probes showed significant wiggling of the pinch. If a pinch wiggle occurs during the imaging of the plasma, then the apparent Zeeman split can be artificially reduced by the lower field strength (less split) spectra impinging on higher field strength chords. To test this theory, ICCD measurements can be retaken with a shorter gate time. If the long gate time is the culprit for the weak magnetic field measurements, then these new measurements with the short gate time should give a higher magnetic field and higher current that agrees more closely with the b-dot data.

4.4 Error/Uncertainty Analysis

Qualitative uncertainty can easily be assessed by looking at the deconvolved parameters from each line in the C IV doublet. A large difference in values found from each of the two lines would suggest large measurement errors since the lines are of the same doublet and ionization state. In the case of ion temperatures, further error can be examined by comparing the temperature measurements from each fiber bundle, as each fiber pair from the two bundles is at the same impact parameter with a difference in axial location or only about a centimeter. Comparing temperatures from each of the two bundles for the 580 nm line proved to be the easiest comparison as the 581 nm line in the doublet was significantly weaker, making deconvolution of the ion temperatures challenging, and sometimes impossible.

Ionization temperature ranges also provide another method of verifying reasonable temperature calculations. Ionization levels generally correspond to specific temperature ranges where certain ionization states will exist in certain fractions within a specific temperature range. Carolan and Piotrowicz created useful plots of ionization states versus electron temperature for a variety of ions. Figure 4.21 shows Carolan and Piotrowicz's ionization calculations for carbon ions. In general, the C IV ion temperatures calculated for these experiments

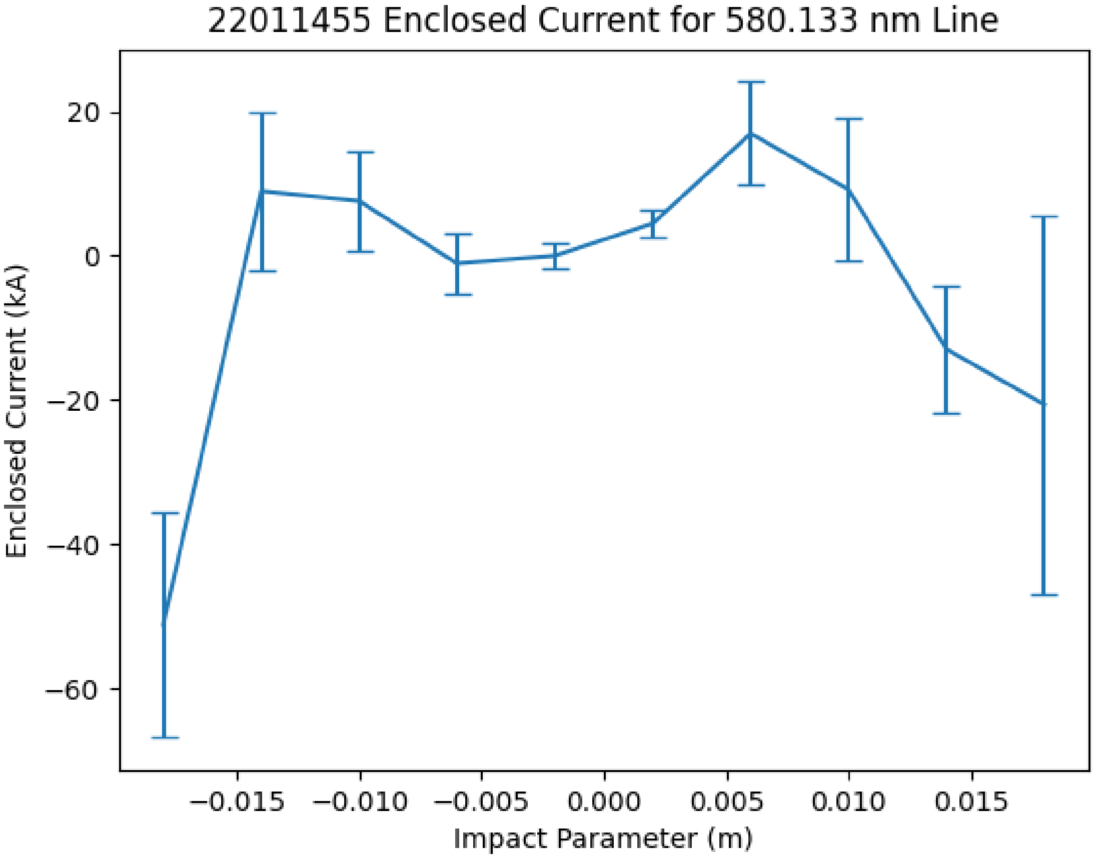

Figure 4.18: A plot of the enclosed current calculation at $T = 45\mu$s. The enclosed current increases with radius, as expected, with a maximum current at the edge of the pinch where all the current has been enclosed. This maximum enclosed current value is then compared with the current measured by the b-dot probes. The nonsensical readings on the far left and far right of the plot are most likely due to weak signals that are difficult to resolve properly at the edge of the spectrometer.

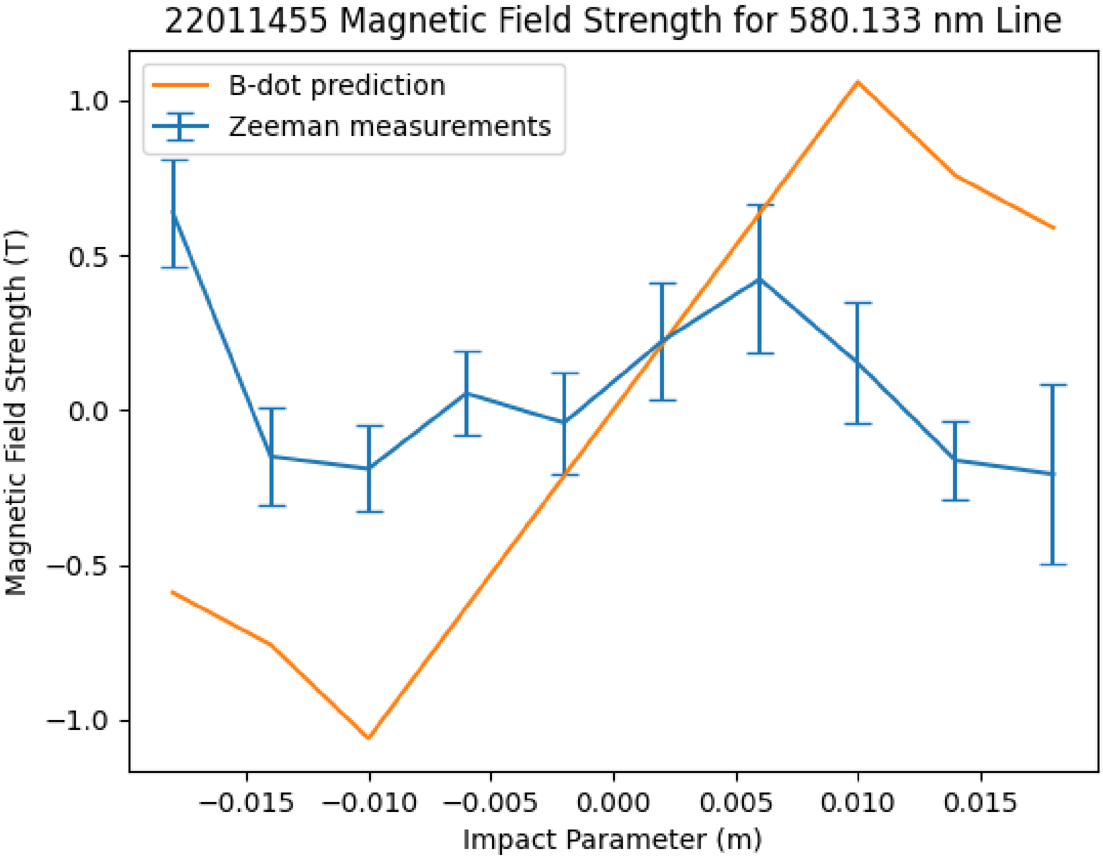

Figure 4.19: A comparison of magnetic field strength as determined by Zeeman splitting and b-dot probes. The large difference in measurements is most likely due to the long exposure time of the ICCD. During this specific pulse, the pinch center location moved by almost two centimeters during the ICCD exposure period. As a result, areas of lower magnetic field strength swept across areas of higher magnetic field strength. This movement reduces the apparent Zeeman split and artificially lowers the magnetic field strength well below the values expected by the b-dot probes.

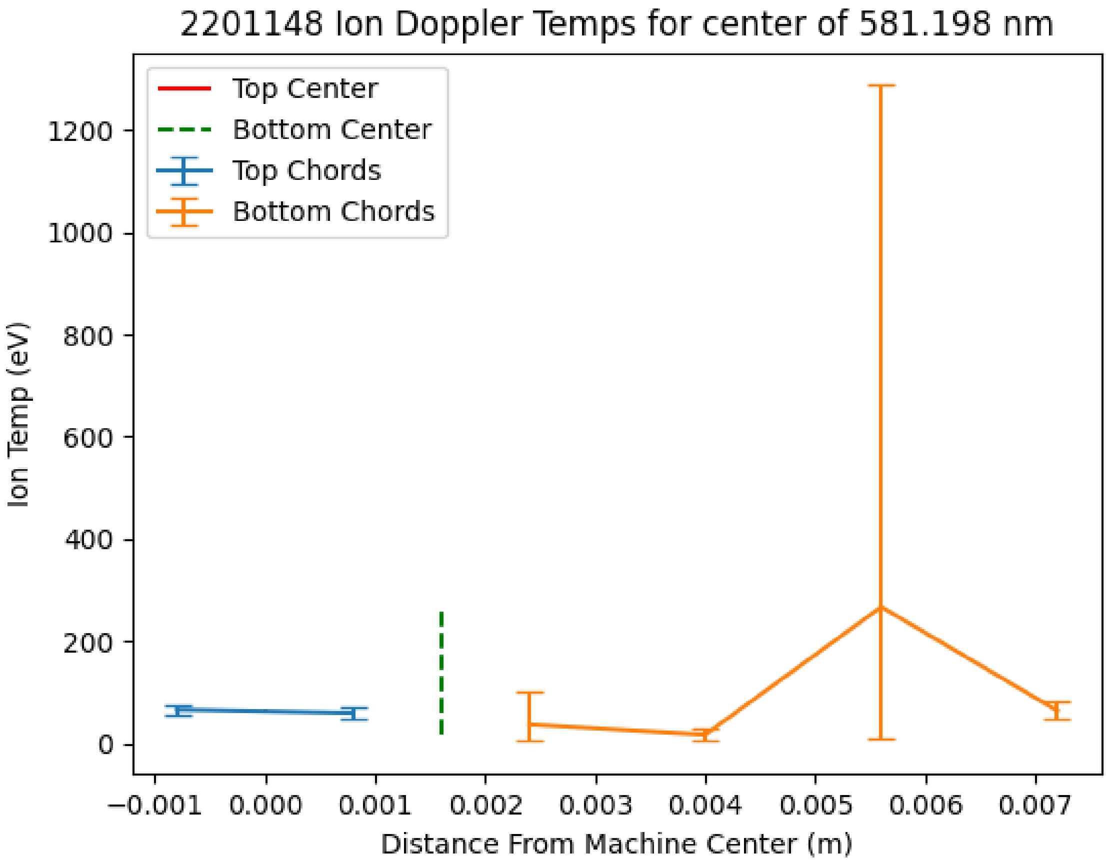

Figure 4.20: An example of attempted deconvolution of ion temperatures for the 581.198 nm C IV line. The weak signals made deconvolving the center temperatures difficult.

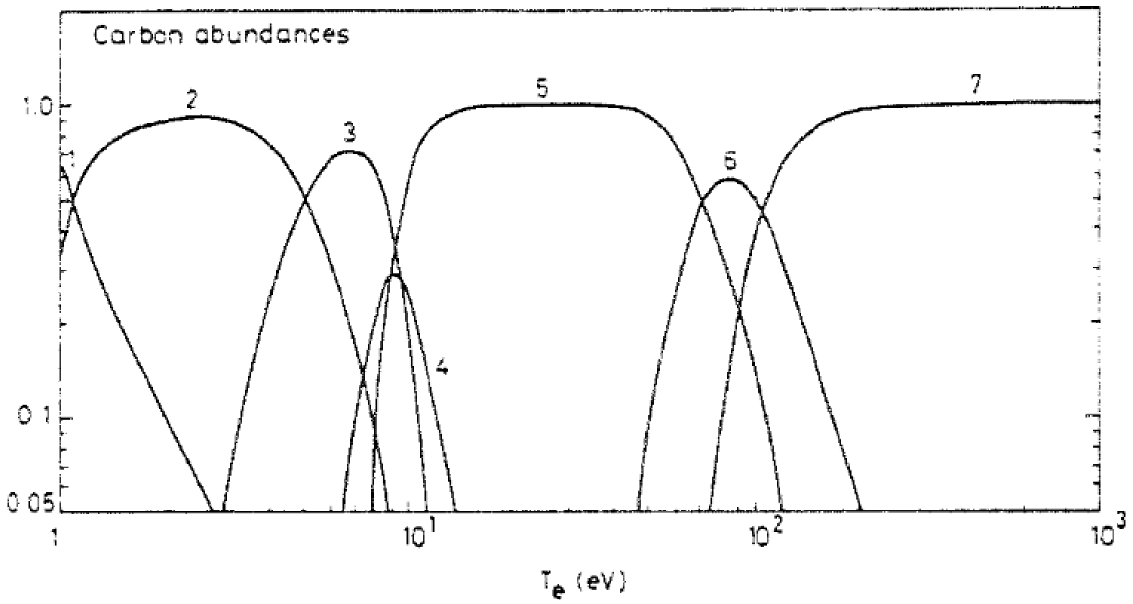

Figure 4.21: Normalized abundance of carbon ionization state with temperature [3]. Note the C IV abundance from 6-20 eV.

lie between 10 and 50 eV. If the ions were assumed to be in local thermodynamic equilibrium with the electrons, then the C IV temperatures on ZaP-HD are somewhat greater the 6 - 20 eV electron temperature range found by Carolan and Piotrowicz. C IV should be completely burned through above 20 eV. Since the C IV signal is visible and measured above 20 eV, there is most likely some artificial broadening effect in play. The long ICCD gate time mixed with the wiggle of the pinch are the likely culprits for this broadening. As the pinch wiggles, the weak-field spectra pass through chords where stronger spectra have just been. The sum of the weaker and strong split give an artificially broadened signal since the centroids of each field strength spectra are shifted slightly in wavelength space. The artificially broadened signal is then interpreted as a higher temperature than the actual plasma temperature.

Confidence intervals for each measurement provided quantitative assessments of measurement uncertainty. For spectroscopic fit, error bars were generated by looking at the goodness of each instrument-broadened Gaussian fit. SciPy's `curve_fit()` function, used for fitting to the binned one-dimensional spectra, outputs a covariance matrix. The square root of each diagonal in the covariance matrix gives the standard deviation of each fit parameter. Multiplying the standard deviation by 2 gives the approximate 95% confidence interval for each parameter. These confidence intervals were then propagated through calculations. Using the goodness of the fit to estimate uncertainty provides a good approximation of uncertainty as good fits will have small uncertainties while poor fits, from weak, noisy signals or from repeated subtracted fits (deconvolution) will have larger uncertainties.

Chapter 5

CONCLUSION

Radially deconvolved ion Doppler temperature and Zeeman splitting measurements were successfully taken for the ZaP-HD SFS Z-pinch experiment during the middle, end, and after the quiescent period of the SFS Z pinch. Two imaging systems where used: a Princeton Instruments Pi-Max, which can take a single, precisely-timed image at one point during the pulse, and a Specialized Imaging Kirana-05M, which can take up to 64 frames at up to 1M FPS. Measurements by the Pi-Max captured the fine structure of the pinch with a high, generally uniform current density across the radius of the pinch. Most of the heating was assumed to be ohmic as the ion temperatures generally trended with localized pinch current.

Due to external circumstances, Kirana measurements where incredibly limited but showed promise for future campaigns. Preliminary measurements showed general agreement with ICCD measurements, but the weak signals significantly reduced the number of resolvable measurements.

Although current measurements were acquired, the current calculated by the ICCD did not match with the current calculated by the magnetic field probes. There was also significant disagreement over the b-dot probe determined pinch center and the spectroscopy determined pinch center. The likely cause for the discrepancy was the long exposure period needed by the ICCD to capture strong spectra signals. The b-dot probes showed large fluctuations in pinch location during some pulses. As a result, ICCD measurements ended up being significantly time-integrated which impacted the deconvolved pinch center and the strength of the Zeeman splitting measurements. For future measurements, the gate width of the ICCD should be minimized as much as possible to ensure that minimum time averaging of the spectra occurs.

Chapter 6

FUTURE WORK

A more significant run campaign with the Kirana should be conducted to provide more statistical significance to time-resolved measurements made on ZaP-HD. The deconvolution scheme had significant trouble resolving the spectra from the Kirana as the signals were quite weak. Unfortunately, due to external circumstances, a second run campaign with dialed-in Kirana settings could not be conducted in time. Another run campaign should be conducted to better determine radially deconvolved ion temperatures and pinch magnetic fields.

A more rigorous error analysis should also be conducted. Although confidence intervals from the goodness of fit gives a good approximation of error and how it increases with weaker signals and deconvolution, they do not include uncertainties of the measuring equipment. Figure 6.1 shows the existence of noise and small measurement errors even in steady calibration data for measurements taken with the ICCD. Filuk and Bailey provide an excellent starting point for analyzing spectroscopy data that contains noise [6]. Golingo and Shumlak apply Filuk and Bailey's work to radial deconvolution by creating a rigorous error analysis of radially deconvolved spectra that should be used for future deconvolution work [11].

Since Zeeman splitting is such a small effect, the magnetic field uncertainty for these measurements was quite high. However, the size of the apparent Zeeman split can be increased by using longer-wavelength spectra since the Zeeman split is proportional to λ_0^2. Spectral surveys during the early portion of this experimental work looked for long wavelength impurities with ionization states in the temperature ranges seen in ZaP-HD. Although there were some candidate oxygen, nitrogen and carbon lines (all known impurities within ZaP-HD), no strong spectra could be resolved with a wavelength longer than the C IV doublet examined

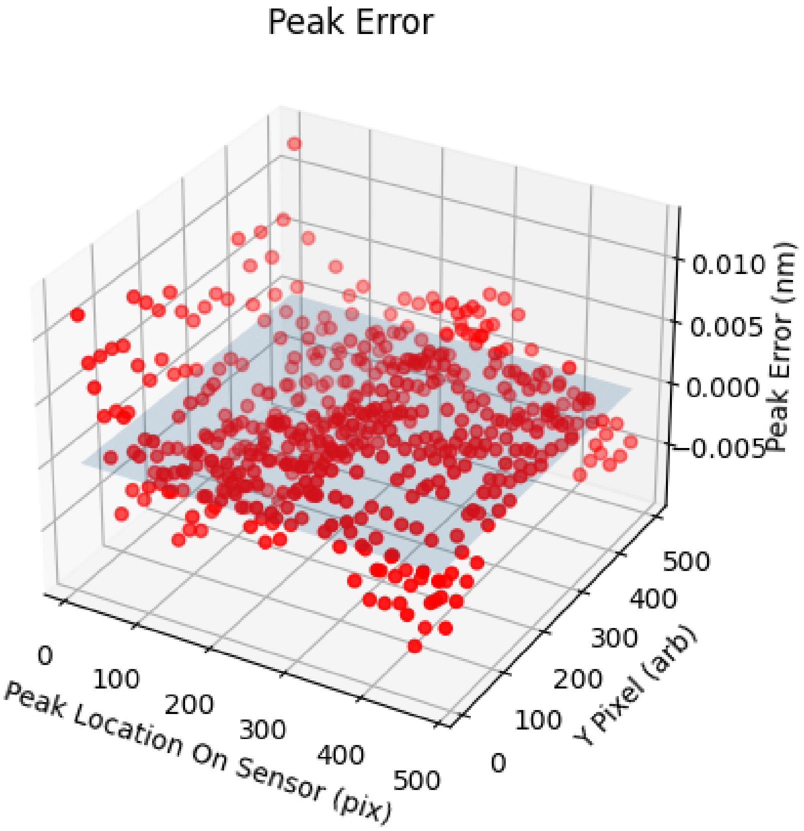

Figure 6.1: Peak errors to calibration data after applying a calibration fit. Although the random errors are on the order of tens of nanometers, the Zeeman split for a 0.6 tesla magnetic field is only about 0.012 nanometers [11].

for this work. However, doping with outside impurities, like the methane used to increase carbon intensity for Kirana measurements, presents a possible way to add longer-wavelength spectra. Argon is affordable, non-reactive, and has many candidate lines in the 600 nm range. Oxygen has a highly ionized line at 650 nm, but its reactivity, especially with metals, and incompatibility with hydrogen make it a candidate only for brief run campaigns at low concentrations with non-hydrogen plasmas.

Another way of dealing with the small split is by using a higher groove density grating with a blaze angle near 500-600 nm. The grating used for these experiments had a visible wavelength blaze angle, but only a groove density of 2400 g/mm. A diffraction grating with a higher groove density blazed for visible light could provide more wavelength dispersion and therefore more precision with resolving Zeeman splitting while still having high enough efficiency to maintain a strong signal.

BIBLIOGRAPHY

[1] Willard H. Bennett. Magnetically Self-Focussing Streams. *Physical Review*, 45(12):890–897, June 1934.

[2] Sayak Bose, Manjit Kaur, Kshitish K. Barada, Joydeep Ghosh, Prabal K. Chattopadhyay, and Rabindranath Pal. Understanding the working of a B-dot probe. *European Journal of Physics*, 40(1):015803, January 2019. arXiv: 2009.10722.

[3] P. G. Carolan and V. A. Piotrowicz. The behaviour of impurities out of coronal equilibrium. *Plasma Physics*, 25(10):1065, 1983.

[4] Daniel Clery. A piece of the sun : the quest for fusion energy, 2013. ISBN: 9781468304930 Place: New York.

[5] Christian Doppler. *Ueber das farbige Licht der Doppelsterne und einiger anderer Gestirne des Himmels: Versuch einer das Bradley'sche Aberrations-Theorem als integrirenden Theil in sich schliessenden allgemeineren Theorie.* K. Böhm Gesellschaft der Wissenschaften, 1903.

[6] Alex B. Filuk and James E. Bailey. Analyzing noisy spectral line shapes. *Review of Scientific Instruments*, 63(10):4783–4785, October 1992.

[7] E. G. Forbes and U. Shumlak. Spatio-temporal ion temperature and velocity measurements in a Z pinch using fast-framing spectroscopy. *Review of Scientific Instruments*, 91(8):083104, August 2020.

[8] Eleanor Forbes. *Diagnostic Development and Plasma-Material Interaction Studies on the ZaP-HD Device.* PhD thesis, University of Washington, 2020.

[9] John L. Giuliani and Robert J. Commisso. A Review of the Gas-Puff Z -Pinch as an X-Ray and Neutron Source. *IEEE Transactions on Plasma Science*, 43(8):2385–2453, August 2015. Conference Name: IEEE Transactions on Plasma Science.

[10] R. P. Golingo and U. Shumlak. Spatial deconvolution technique to obtain velocity profiles from chord integrated spectra. *Review of Scientific Instruments*, 74(4):2332–2337, April 2003.

[11] R. P. Golingo, U. Shumlak, and D. J. Den Hartog. Note: Zeeman splitting measurements in a high-temperature plasma. *Review of Scientific Instruments*, 81(12):126104, December 2010.

[12] Raymond Golingo. *Formation of a sheared flow Z -pinch.* Ph.D., University of Washington, Seattle, 2003. ISBN: 978-0-496-58598-4 Publication Title: ProQuest Dissertations and Theses 3111068.

[13] D.A. Gurnett and A. Bhattacharjee. *Introduction to Plasma Physics: With Space, Laboratory and Astrophysical Applications.* Cambridge University Press, 2017.

[14] Daniel Hartog. How to set up and use the ICCD viewing telescopes on ZaP, July 2000.

[15] Aaron Hossack. *A Study of Plasma Dynamics in HIT-SI using Ion Doppler Spectroscopy.* Thesis, University of Washington, 2015. Accepted: 2015-09-29T17:56:18Z.

[16] I.H. Hutchinson. *Principles of Plasma Diagnostics.* Cambridge University Press, 2002.

[17] S. Jackson, U. Shumlak, B. Nelson, R. Golingo, R. Lilly, and T. Shreve. Effects of Initial Gas Injection on the Behavior of a Sheared-Flow Z-Pinch. In *41st AIAA/ASME/SAE/ASEE Joint Propulsion Conference & Exhibit*, Tucson, Arizona, July 2005. American Institute of Aeronautics and Astronautics.

[18] S. L. Jackson and U. Shumlak. Abel inversion of a holographic interferogram for determination of the density profile of a sheared-flow Z pinch. *Review of Scientific Instruments*, 77(8):083502, August 2006.

[19] F. C. Jahoda, F. L. Ribe, and G. A. Sawyer. Zeeman-Effect Magnetic Field Measurement of a High-Temperature Plasma. *Physical Review*, 131(1):24–29, July 1963.

[20] B. B. Kadomtsev. Hydromagnetic stability of a plasma. *Reviews of plasma physics*, 2:153–199, 1966. Publisher: Consultants bureau New York.

[21] Amierul Aqil bin Khairi. *Graphite Electrode Characterization on the ZaP-HD Sheared-Flow-Stabilized Z-Pinch Device.* Thesis, University of Washington, 2021. Accepted: 2021-10-29T16:17:22Z.

[22] J. D. Lawson. Some Criteria for a Power Producing Thermonuclear Reactor. *Proceedings of the Physical Society. Section B*, 70(1):6–10, January 1957.

[23] Timothy Joseph Lloyd. *Comparison of Diagnostics for Determining Z Pinch Centroid in the ZaP-HD Experiment.* Thesis, University of Washington, 2022. Accepted: 2022-04-19T23:41:59Z.

[24] Lorcan Padraig Joseph McGonigle. *Simultaneous Spectroscopic Determination of Ion Temperature, Electron Density, and Magnetic Field for the ZaP-HD Experiment.* Thesis, University of Washington, 2015. Accepted: 2015-09-29T17:56:16Z.

[25] J.R. Roberts. Optical-Emission Spectroscopy on the Gaseous Electronics Conference Rf Reference Cell. *Journal of Research of the National Institute of Standards and Technology*, 100(4):353, July 1995.

[26] Michael Patrick Ross. *Exploring plasma stability and confinement with high resolution density measurements on the ZaP-HD Flow Z-Pinch.* Thesis, University of Washington, October 2016. Accepted: 2017-02-14T22:36:05Z.

[27] T. Shikama and P. M. Bellan. Development of a polarization resolved spectroscopic diagnostic for measurements of the vector magnetic field in the Caltech coaxial magnetized plasma jet experiment. *Review of Scientific Instruments*, 84(2):023507, February 2013.

[28] U. Shumlak. Z-pinch fusion. *Journal of Applied Physics*, 127(20):200901, May 2020.

[29] U. Shumlak, C.S. Adams, J.M. Blakely, B.-J. Chan, R.P. Golingo, S.D. Knecht, B.A. Nelson, R.J. Oberto, M.R. Sybouts, and G.V. Vogman. Equilibrium, flow shear and stability measurements in the Z-pinch. *Nuclear Fusion*, 49(7):075039, July 2009.

[30] U. Shumlak and C. W. Hartman. Sheared Flow Stabilization of the m = 1 Kink Mode in Z Pinches. *Physical Review Letters*, 75(18):3285–3288, October 1995.

[31] U. Shumlak, R. Lilly, C. Adams, R. Golingo, S. Jackson, S. Knecht, and B. Nelson. Advanced Space Propulsion Based on the Flow-Stabilized Z-Pinch Fusion Concept. In *42nd AIAA/ASME/SAE/ASEE Joint Propulsion Conference & Exhibit*, Sacramento, California, July 2006. American Institute of Aeronautics and Astronautics.

[32] U. Shumlak, B. A. Nelson, E. L. Claveau, E. G. Forbes, R. P. Golingo, M. C. Hughes, R. J. Oberto, M. P. Ross, and T. R. Weber. Increasing plasma parameters using sheared flow stabilization of a Z-pinch. *Physics of Plasmas*, 24(5):055702, May 2017.

[33] Uri Shumlak. AA 405: Introduction to Aerospace Plasmas.

[34] G. V. Vogman and U. Shumlak. Deconvolution of Stark broadened spectra for multipoint density measurements in a flow Z-pinch. *Review of Scientific Instruments*, 82(10):103504, October 2011.

[35] Simon Woodruff, Ronald Miller, Desmond Chan, Steve Routh, Sakti Basu, and Shankar Rao. *Conceptual Cost Study for a Fusion Power Plant Based on Four Technologies from the DOE ARPA-E ALPHA Program.* Department of Energy, July 2017.

[36] P. Zeeman. The Effect of Magnetisation on the Nature of Light Emitted by a Substance. *Nature*, 55(1424):347–347, February 1897. Bandiera_abtest: a Cg_type: Nature Research Journals Number: 1424 Primary_atype: News Publisher: Nature Publishing Group.